Modelling the Last Glacial Ice Sheet on Antarctica

With Laterally Varying Relaxation Time

D.F. Oude Egbrink

Delft University of Technology

TU Delft

Modelling the Last Glacial Ice Sheet on Antarctica

with Laterally Variable Relaxation Time

by

D.F. Oude Egbrink

to obtain the degree of Master of Science
in Aerospace Engineering
at the Delft University of Technology,
to be defended publicly on Thursday December 21, 2017 at 10:00 AM.

Student number:	4150392	
Project duration:	April 1, 2017 – December 21, 2017	
Thesis committee:	Dr. L.L.A. Vermeersen	TU Delft
	Dr. ir. W. van der Wal	TU Delft
	Dr. ir. C.C. de Visser	TU Delft
	Dr. R. S. W. van de Wal	IMAU, Utrecht University
	Dr. B. de Boer	IMAU, Utrecht University

This thesis is confidential and cannot be made public until December 21, 2017.

TU Delft

Preface

On the 12th of December 2015, 196 parties signed the *Accord de Paris*, aimed to keep global temperature rise this century below 2 degrees Celsius above pre-industrial levels. We are currently on track to reach an increase of 4 degrees Celsius by the end the century. The accord is a step in the right direction, but we all must contribute to solve this immense problem.

We are the last best hope of Earth. You and I must protect it, Or we – and all living things we love – are history.

I hope that this thesis adds to our understanding of the planet Earth.

D.F. Oude Egbrink
Delft, December 2017

Acknowledgements

During the course of this research assignment, many people have been very helpful. First and foremost, I would like to thank my daily supervisor Dr. Ir. Wouter van der Wal. Besides giving me guidance and structure during this assignment, he gave me very useful insight concerning the relevant topics of this thesis. I see Wouter as a very skilled researcher, but more importantly, as a very kind person.

Furthermore, I would like to express my gratitude to Dr. Bas de Boer at the Institute of Marine and Atmospheric research Utrecht (IMAU), who not only provided the ANICE computer model, but also provided very useful feedback during several meetings in person and via Skype. Next to that, his responses to my numerous emails were always fast and loaded with useful information. Pablo Vizcaino Rubio has been very useful in the initial state of this research, by showing me the ins and outs of the ANICE computer model. He provided me with schematic set-ups that were very useful in becoming familiar with the model. Dr. Roderik van de Wal from the Institute of Marine and Atmospheric research Utrecht (IMAU) was most helpful by giving me input during a number of meetings in Utrecht and via Skype. Dr. Pippa Whitehouse was kind enough to provide several viscosity models that were used in this research. Next to that, she provided region boundary sets, which saved me from a lot of manual work, for which I want to thank her.

Finally, I wish to thank my family, and in particular my parents, for always showing a sincere interest in my research.

Abstract

Glacial isostatic adjustment is the viscoelastic response of the earth to loading. Ice dynamic models employ glacial isostatic adjustment computations to accurately simulate ice sheet development, because it can greatly affect ice sheet development. Ice dynamic models assume a laterally constant relaxation time to simulate bedrock uplift. However, shear wave velocity data suggest a sharp increase in relaxation time between West and East Antarctica. This signifies the importance of using an laterally varying relaxation time. In this study the aim is to improve an ice dynamic model by using a laterally varying bedrock relaxation time.

Viscosity values from shear wave velocities are used to create laterally varying relaxation time maps for Antarctica. Five regions in Antarctica were identified for which wavelength dependent bedrock uplift curves were generated, using a normal mode model. These complex uplift curves were converted to relaxation time fields by fitting the dominant uplift modes to a simple exponential curve. The resulting relaxation time fields can be used in an ice dynamic model but are a simplification of the complex mantle viscosity profile. Four different relaxation time fields followed from the viscosity conversion, where values differ up to two orders of magnitude compared to the widely used constant relaxation time (of 3000 years). The ice dynamic model was adjusted to enable for laterally varying relaxation time maps. Furthermore, the model was adjusted to allow for relaxation time adjustment to ice sheet wavelength in each region. Using these adjustments, one reference model and four selected models were used in an ice dynamic simulation where the Antarctic Ice Sheet was simulated from 120 000 kyr ago to PD (De Boer, 2014).

It was found that the different models showed the same ice volume development in the build-up phase of the last glacial. In the melt epoch that occurred from 20 000 years ago up to PD, the different models showed diverging ice volumes: the model with on average high relaxation times showed a decrease in ice volume of 22.0%, whereas the model with on average low relaxation times decreased by 17.4%. The ice volume difference between these two models is equal to 3.5 m SLEQ at PD. All models estimate the ice volume at PD well below the current Bedmap2 estimate of 26.92 million km^3, where the low relaxation time model is closest with 25.28 million km^3. The high relaxation time model gives worst performance with 23.93 km^3. It was found that the largest differences between the models occurred at the WAIS due to the close relationship of sea level and bedrock uplift. Uplifting bedrock shallows the local sea level and forces quicker grounding of ice shelves which prevents further melt along the base. It was shown that during the last -20 000 years, reduction of grounded ice in several regions lead to reduced wavelengths of ice sheets. This reduction in wavelength led to smaller relaxation time values for all regions. It appeared to be a stabilising mechanism for decreasing ice sheets. It was clearly seen for the Ross ice shelf, but less obvious for the Ronne ice shelf, partially due to inconsistent model behaviour. In was shown that relaxation time changes dynamically with changing ice sheet wavelengths. However, additional research is required to show how significant this behaviour is.

Contents

List of Figures

List of Tables

List of Abbreviations

AIS Antarctic Ice Sheet

EAIS East Antarctic Ice Sheet

ELRA Elastic Lithosphere - Relaxing Asthenosphere

GIA Glacial Isostatic Adjustment

kyr kiloyear - one thousand years

LGM Last Glacial Maximum

NAP North Antarctic Penninsula

PD Present Day

SLEQ Sea Level Equivalent

SLHE Schaeffer and Lebedev - Heeszel

WAIS West Antarctic Ice Sheet

1

Introduction

In this chapter the topic of this thesis will be introduced. A small introduction will be given to a few of the many subjects that this thesis touches upon. In section 1.1 the study of glaciation and deglaciation of earth will be discussed. The forcing and feedback mechanisms of ice ages will be discussed. The region of interest, Antarctica, will be more broadly examined in section 1.2. In this section the behaviour of Antarctica throughout several (de)glaciation cycles will be discussed, as well as the interesting differences between east and west Antarctica. Also in this section, the reader will be briefly introduced to the computer model that is used to model the Antarctic ice sheets through the last glaciation period. It is the model that is used to perform all the necessary computations for this thesis. After that, Glacial Isostatic Adjustment, or GIA, will be introduced in section 1.3. It is the main phenomenon on which this thesis is built.

1.1. Glaciation and Deglaciation

Ice ages are considered to be periods where the temperature on earth is reduced. This reduction of temperature leads to the presence of polar ice sheets. Within an ice age, relatively cold and warm periods occur, which are referred to as glacials and interglacials. Ice ages have occurred on this planet throughout history. They are the cause for several geographic as well as paleo-climatic events. Evidence shows that there must have been at least five major ice ages in Earth's history (Muller and MacDonald, 2000).

The occurrence of glacials and interglacials is subject to a number of causes and effects, which can be divided into astronomical forcing and feedbacks. Astronomical causes are found in small alterations of the earth's orbit. The combination of varying eccentricity, obliquity, and precession leads to a complex periodic signal that is often referred to as the Milankovitch cycles. These cycles prescribe the solar radiation pattern over time that leads to variation in solar energy that reaches the earth (Muller and MacDonald, 2000). Next to the Milankovitch cycles that induce varying insolation, several mechanisms naturally exist that enable or respond to changing climate factors.

The Earth's albedo has a positive feedback on climatic changes as ice sheets generally have a high albedo and thus a high reflectivity. This will cause a reduction in absorbed solar radiation and consequently, lower temperatures (which will induce ice sheet grow).A negative feedback is the reduction of precipitation during glacials, which reduces the availability of snow to maintain the ice sheet. In extreme cases, the ice sheet advances towards low latitudes, covering large parts of continental bed. This inhibits photosynthesis, which in turn increases CO_2. Next to that it inhibits silicate weathering, which in turn also increases the amount of CO_2 in the atmosphere (L. Kirschvink, 1992). As CO_2 is a greenhouse gas, the increase of concentration would increase the temperature, and hence, decrease ice sheet growth. Next, Glacial Isostatic Adjustment (GIA) also provides a feedback system for emerging or collapsing ice sheets, but this topic will be discussed later.

The first ice age, the Huronian, dates from 2.4 billion years ago and lasted about 300 million years. After this, four more ice ages occurred. The last - which is also the current ice age - is the Quaternary. This ice age started 2.6 million years ago and has not ended yet, due to the existing ice caps at both the south and north polar regions. In the last ice age several periods of glaciation and deglaciation existed, of which the last glaciation period lasted from 110,000 years ago to about 11,700 years ago (Ehlers et al., 2015). In this period, around 21 to 27 kyr BP (kiloyear before present), the ice caps where at their maximum volume, hence it is called the Last Glacial Maximum (LGM). There is no clear consensus on the exact time of the LGM.

1.2. The Continent Antarctica

One of the last existing ice caps at present day is located on the Antarctic continent. Antarctica is the least populated continent on earth and one should not underestimate some of the good reasons for this. Number one reason is the climate: it has the coldest, driest and most windy climate of all continents. Annual precipitation in coastal regions is up to 200 mm (The Netherlands has a yearly value of 800 mm), but this value decreases quickly when going inland. Temperatures reach up 5 °C - 15°C along the coast during summer. This might seem endurable, but the coldest temperature measured ranges between -80°C and -89.2 °C (Liggett et al., 2016). Antarctica is basically a frozen desert. If you are, despite aforementioned harsh conditions, interested in building a life on Antarctica, you can consider yourself lucky. Several permanent research stations are based on Antarctica, albeit close to the shore. Population is up to 5000 residents during summer, but when winter starts, most residents flee the imminent cold. If your aim is to become the first parent to a child born on the continent, I must disappoint you. Already up to ten children have been born on Antarctica (Liggett et al., 2016).

On a more serious note, Antartica is a permanent ice sheet on the most southern continent. The Antarctic Ice Sheet (AIS) can be divided into the East Antarctic Ice Sheet (EAIS) and the West Antarctic Ice Sheet (WAIS), where the division is formed by the Transantarctic Mountain region. The EAIS is the most stable ice sheet and ice sheet thickness goes up to about 5 km inland. It is almost completely situated on continental land mass. In contrary, the WAIS remains on bedrock mostly below sea level. It is considered to be an unstable ice sheet because of this. The WAIS features two large ice shelves: The Ross Ice Shelf and the Filchner-Ronne Ice Shelf (in this work referred to as the Ronne Ice Shelf). During the last melt epoch that started after LGM, nearly all mass loss occurred at the WAIS (Liggett et al., 2016).

Over the last decades, a lot of research has been done about the stability of the WAIS and to what extend human climate interaction can cause a (partial) collapse of this ice sheet (Bamber et al., 2009; Joughin et al., 2014; Scambos et al., 2004; Thomas, 2004). In order to determine what will happen in the future, the behavioural history of the complete ice sheet must be fully understood. In this thesis, a computer model will be used to model the Antarctic Ice Sheet from the last -120 000 up to Present Day (PD). It will focus on the dynamics of the ice sheet and more specific, the effect of variable bedrock adjustment. This will be discussed in the next section.

1.3. Glacial Isostatic Adjustment and the Ice Dynamic Models

Glacial Isostatic Adjustment, or GIA, also known as post-glacial rebound, is the phenomenon that occurs during and after an ice sheet exerts loading on the earth's mantle. As with most materials, there is some deformation after a force is applied to it. Being it plastic or elastic, the material shows some form of shape change. And sometimes, this shape change does not occur instantly, but only after some time. Take for example a jar of honey. Lay a spoon on the surface, and it takes a while before it is completely submerged. For the earth, the same holds. When a relatively large load, like an ice sheet, is placed upon the earth, the earth responds to such a loading. In a timely manner, the underlying bedrock will deflect towards a new equilibrium state. When such a large loading disappears, for example during a large melt epoch, the bedrock will re-adjust back to its original position. The time in which this bedrock adjustment happens, can range from a few decades to thirty-thousand years in Antarctica (Whitehouse et al., 2017b).

Including bedrock relaxation in the ice model influences the development of the ice sheet in many ways. There are two main reasons why GIA influences ice dynamics: first, bedrock adjustment affects the ice sheet surface elevation. The decrease of surface elevation will result in more melt and hence, a lower mass balance, which reduces surface elevation even more (Le Meur and Huybrechts, 1996). Second: the ice sheet development in the marine sectors of the Antarctic Ice Sheet is highly dependent on local sea level (Mercer, 1978; Schoof, 2007; Weertman, 1974). A fast rebound of the underlying bedrock during ice sheet retreat shallows the sea level and lowers the amount of ice flux towards to oceans in those regions. This prevents severe mass loss in the ice sheet regions further upstream (Feldmann and Levermann, 2015; Gomez et al., 2015, 2013; Huybrechts, 1990). This amplifies the importance of including detailed Antarctic bedrock properties as well as local sea level for accurate modelling of the AIS.

It is known that the Antarctic bedrock has varying properties with position. Specifically, a distinct separation in mantle viscosity is observed between east and west Antarctica (An et al., 2015; Heeszel et al., 2016; Kaufmann et al., 2005; Morelli and Danesi, 2004). Moreover, mantle viscosity is strongly correlated to the relaxation time of the bedrock. The bedrock adjustment under the EAIS is considered to have slow bedrock relaxation, whereas the WAIS bedrock relaxation is mostly considered fast.
There is a broad range in models that simulate the Antarctic ice sheet history. Up till now, coupled Antarctic ice sheet-bedrock models have only been used where the bedrock properties are *laterally* varying, but the used ice model is *static* (Geruo et al., 2013; Kaufmann et al., 2005; Sabadini et al., 1986; Spada et al., 2006; van der Wal et al., 2015). On the other hand, studies have used a *dynamic* ice model, but the underlying earth is modelled using an *only radially varying* SVGE model (De Boer, 2014; Le Meur and Hindmarsh, 2001; Le Meur and Huybrechts, 1996) or an ELRA model with *constant*

relaxation time (Gomez et al., 2013; Le Meur and Huybrechts, 1996; Whitehouse et al., 2012). In these models the laterally varying properties in Antarctica are neglected. Ice *dynamic* models have not been used in combination with a *laterally variable* relaxation time. The aim of this thesis is to include such a laterally variable adjustment, and, more importantly, discuss the effects of such implementation on the ice sheet development of the EAIS and the WAIS in an ice dynamic model.

1.4. Research Questions

To conclude this introduction, the research questions are stated. They follow from the previously shown literature and the knowledge gap in it.

1. How can an existing ice dynamic model be improved using laterally varying bedrock adjustment properties?
    (a) How can a laterally varying relaxation time be integrated into an ice dynamic model?
    (b) How is a 3D varying viscosity field converted to a 2D relaxation time field?
        i. How does the wavelength of an ice sheet affect the excited deformation of the viscosity at different depths?
        ii. How does a complex bedrock uplift curve relate to a single relaxation time?
2. How do the results of an ice dynamic model with a *laterally* varying relaxation time compare to a benchmark model and to the existing literature?
    (a) How do ice thickness and ice volume of the Antarctic ice sheet develop during the last glacial cycle using a laterally varying relaxation time?
    (b) What are the differences in the stability of the AIS and in particular the WAIS, for different relaxation time models?

1.5. A Note on the Structure of the Thesis

Here, the writer of this report will give a small note on the structure of this thesis. As the thesis touches upon a few different, maybe seemingly unrelated topics, it might be confusing for the reader who is not familiar with this subject. The structure of this thesis is more or less chronologically to the research assignment. Therefore, the thesis will start with a discussion on the ice model that has been used throughout the assignment in chapter 2. In chapter 3, a specific part of the ice dynamic model will be modified in order to allow for more consistent sea level forcing. This modification concludes the ice dynamic modelling part and a new topic is introduced in chapter 4: bedrock viscosity and relaxation times in Antarctica. A large part of the thesis consists of converting the complex mantle viscosity fields to a relaxation time field that can be used in the ice dynamic model.

A set of relaxation time fields that are generated by converting different mantle viscosity fields in chapter 4, are used in the ice-dynamic model. This will lead to a series of results, that are presented in chapter 5. These different results are compared and the important findings are discussed in chapter 6. Lastly, in chapter 7, the research questions are answered and the results are reviewed upon with respect to known literature.

2

Modelling of the Antarctic Ice Sheet with the ANICE Computer Model

In this chapter, a broad introduction will be given to the computer model that is used for the simulations. An overview of the different methods in the ice dynamic computer model will be given in section 2.1. Next to that, the eustatic sea level forcing and temperature forcing will be showed, as well as several other forcing fields. The bedrock uplift method that calculates GIA will be discussed more in depth in section 2.2. In section 2.3, the standard run of the ice dynamic model will be shown.

2.1. The Ice Dynamic ANICE Model and its Forcing Fields

The ANICE computer model is an ice dynamic model that enables the user to simulate one or multiple ice sheets through time. It was provided by Dr. B. de Boer[1] to be used in this research. In order to understand the outcome of such a simulation, the user must be familiar with the ice dynamic equations that are being used within the model. Therefore, a description will follow that explains the main ice sheet dynamics. The ice sheet dynamics shown below are a description of the mathematical code of the ANICE model. In this work, the ANICE computer model is used to solely model the Antarctic Ice Sheet. The model computes the state of the AIS, with a global time step of 100 years, from a point in history up to PD. The grid consists of 141 by 141 points with a gridsize of 40 km, covering an area of 32 million km^2.

2.1.1. Physical Description of Ice Sheets

A large ice mass like Antarctica consist of the main part which is referred to as the ice sheet. This part rests on underlying bedrock and is therefore *grounded*. At the ice sheet margins, ice shelfs form. These are masses of ice that do not rest on bedrock but instead float on water. The grounding line forms the separation between ice sheets and shelves. An ice sheet maintains its mass through a net accumulation of mass throughout a mean year (Schoof and Hewitt, 2013). At the centre of the ice

---

[1] Dr. B. de Boer, Institute for Marine and Atmospheric research Utrecht (IMAU), Utrecht University

sheet, mass balance is mostly positive through precipitation, whereas at the margins mass decrease occurs through melt and ablation. Internally, mass transportation happens from the centre of the ice sheet towards the ice sheet margins. Combining the mass balance and internal velocities gives the following differential equation for the ice height (van der Veen, 1999):

$$\frac{\partial H_i}{\partial t} = -\nabla \cdot (H_i \mathbf{u}) + B. \tag{2.1}$$

H_i is the ice height in meters, t is time, $\mathbf{u}$ is the vertically integrated horizontal velocity profile in meters per second, and B is the mass balance in meters ice equivalent per unit time. Below, the used methods to compute the different terms in Equation 2.1 are described as used in the ANICE computer model. For in-depth discussions of the governing equations, please refer to Appendix A.

Mass Increase through Precipitation and Refreezing

Accumulation of ice sheet mass happens through several processes. The main source is dry precipitation in the form of snow (van der Veen, 1999). The value of precitipation is mainly dependent on the condensation temperature above the inversion layer, which in turn is proportional to the atmospheric moisture content (Huybrechts, 2002). Furthermore, accumulation by refreezing of meltwater and rain is included in the model by a method described in Janssens and Huybrechts (2000), where the refreezing is dependent on the surface temperature, available melt water, and retention potential.

Mass Loss through Ablation and Basal Melt

Basal melt at the ice shelves induced by ocean water is included by using a combination of the parametrisation method described in Pollard and Deconto (2009) and a temperature based method described in Martin et al. (2011). The combined method calculates the basal melt at the shelf as a function of temperature, insolation, depth of the ocean, heat transfer between ocean and shelf, and others factors. Ablation is the mass loss that happens at the margins of the ice sheet. It is based on present day mass balance observations in Antarctica en Greenland. It is a parametrisation based on incoming radiation and temperature (Bintanja et al., 2002; van den Berg et al., 2008a).

Internal Mass Transportation

Externally, the mass balances are affected by accumulation and melt. Internally the ice sheet deforms as well. Under influence of pressure and friction, mass transport inside the ice sheet moves particles from central parts to the ice sheet margins. The ice sheet dynamics that govern this mass transport are modelled through two models: The shallow ice approximation (SIA), and the shallow shelf approximation (SSA). SIA is used for central parts of the ice sheet, where horizontal shear stress is assumed to be large compared to to normal stresses and longitudinal stresses. SIA is used in the regions along the ice sheet margins. Here, longitudinal stresses become larger with respect to the horizontal shear stress, and the shallow ice approximation does not hold anymore. If the reader wishes to get more information about the governing equations for SSA and SIA, please refer to Appendix A.

2.1.2. Forcing of the ANICE Model

The standard ANICE model is forced by eustatic sea level and temperature variations relative to present day values. In Figure 2.1, the temperature (top) and eustatic sea level (bottom) forcing is shown for the last 120 000 years. The sea level values are constant for the entire grid and do not vary locally, only temporally. The temperature and sea level values are based on global simulations of 1-D ice sheet models which were forced by benthic δ^{18}O records (De Boer et al., 2010).

Next to the main eustatic sea level and temperature forcing, several fields are used as input forcing that do vary laterally. The heat flux input field describes the average solar flux that is received at all grid-points in the model. Next to the heat flux, also a monthly precipitation field is used as input. The precipitation field prescribes the amount of monthly dry and wet perception at all locations. Lastly, the monthly air temperature variation at 2 meter above the surface is used as an input for the model. The initial conditions (at -120 000 years) are a set of fields that describe the AIS at PD, because the ice volume at PD is comparable to that of the ice volume at -120 kyr ago.

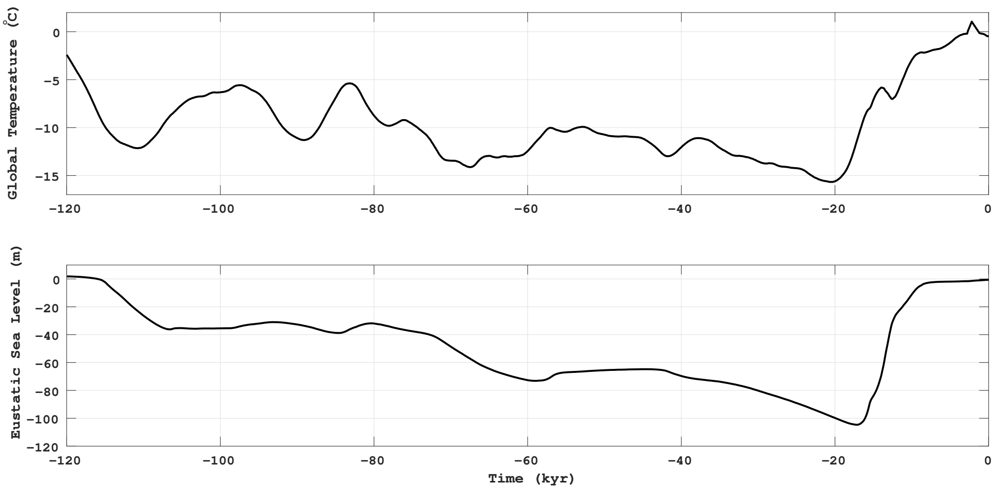

Figure 2.1: Forcing curves for temperature (top) and eustatic sea-level (bottom).

2.2. Glacial Isostatic Adjustment Methods and ANICE

Glacial Isostatic Adjustment is one of the main subjects in this thesis. It is of importance that GIA is taken into account for a dynamic ice model. GIA can account for large deformations in the bedrock and imposes variation on the ice sheet surface as well, as discussed in section 1.3. Several methods are used for modelling GIA, where the basic methods find their fundament in dividing the complex earth into two layers: the lithosphere and the asthenosphere. In these methods, the lithosphere is non-vicious and has instant deformation, whereas the asthenosphere is assumed to be vicious and deformation is time-dependent. More complex models have also been developed, that account for the multi-layered earth composition (Le Meur and Huybrechts, 1996). The most important models are discussed below.

2.2.1. Different Methods for GIA Calculations

For the lithosphere layer, two main methods exist. The local lithosphere (LL) model neglects flexural rigidity and only accounts for loads on a local level. The elastic lithosphere (EL) model does take flexural rigidity into account which leads to a more physically correct deformation profile. The LL model is found to be inaccurate and the EL model is preferred in order to accurately model the main uplift features (Fjeldskaar and Cathles, 1991; Lambeck et al., 1990; Le Meur and Huybrechts, 1996).

The asthenosphere layer is mainly approximated by two methods as well. The relaxing asthenosphere (RA) assumes an exponential decaying function for the asthenosphere response. The diffuse asthenosphere (DA) is more physically correct by taking into account the diffusion equation for mantle movement. However, Le Meur and Huybrechts (1996) showed that the RA model is more accurate in modelling the response compared to the DA model.

The self-gravitating viscoelastic spherical Earth model (SVGE) is a model that considers the complete earth composition: an inviscid core, a viscoelastic lower and upper mantle, and an elastic lithosphere (Le Meur, 1996). To account for the complex interactions between gravity field perturbations and displacements, the earth is decomposed into spherical harmonics (Peltier, 1974, 1982; Wu and Peltier, 1982).

The SVGE model is computationally more extensive, but does account for the interaction between deformation and gravity perturbations. Le Meur and Huybrechts (1996) argue that the ELRA model provides a reasonable alternative with respect to the SVGE model when comparing time-dependent and geographic behaviour. In the ANICE model, the ELRA model is used to compute the bedrock adjustment. In the next section, this method will be further analysed.

2.2.2. Elastic Lithosphere Theory

The elastic lithosphere model assumes the lithosphere to be a thin plate. Not only the local load is considered, but the contributions from remote locations are taken into account. The downward steady state deflection w_{ss} can be written in differential form (Greve and Blatter, 2013; Le Meur and Huybrechts, 1996):

$$K_1 \nabla^4 w_{ss} + \rho_a g w_{ss} = \rho_i g H_i. \tag{2.2}$$

Here, K_1 is the flexural stiffness, $\rho_i g H_i$ is the ice sheet loading, $\rho_a g w_{ss}$ is the buoyancy force exerted by the asthenosphere on the deflected part of the lithosphere. K_1 can be written as

$$K_1 = \frac{EH^3}{12(1-\nu^2)} = \frac{\mu_s H^3}{6(1-\nu)}, \tag{2.3}$$

where E is Young's modulus, H is the thickness, ν is Poisson's ratio and μ_s is the shear modulus. All variables in Equation 2.3 refer to the lithosphere proporties.

The load $\rho_i g H_i$ is localised through

$$\rho_i g H_i(x,y) = F_0\,\delta(x-\check{x})\,\delta(y-\check{y}) \tag{2.4}$$

where F_0 is the single force equivalent that is acting on the lithosphere at position $(\check{x},\check{y})$. $\delta(x-\check{x})\,\delta(y-\check{y})$ is Dirac's function for an singular force at $(\check{x},\check{y})$. Using Equation 2.4, the solution to the linear differential Equation 2.2 looks like:

$$w_{ss}(r) = -\frac{F_0 L_r^2}{2\pi K_1}\,\mathrm{kei}\left(\frac{r}{L_r}\right), \tag{2.5}$$

where

$$r = \sqrt{(x-\check{x})^2 + (y-\check{y})^2}, \qquad L_r = \left(\frac{K_1}{\rho_a g}\right)^{\frac{1}{4}}. \tag{2.6}$$

Kei is a Kelvin 0th order function. Figure 2.2 shows the behaviour of the kei() function by showing y = kei(x). L_r is called the radius of relative stiffness and is a measure for the non-locality of the lithospheric displacement. at approx. $r = 4L_r$, the lithospheric response goes to zero, after which a small bulge appears (Greve and Blatter, 2013). The first term ($-\frac{F_0 L_r^2}{2\pi K_1}$) of Equation 2.5 defines the amplitude of the curve in Figure 2.2, whereas the Kei function in Equation 2.5 defines the shape of the curve.

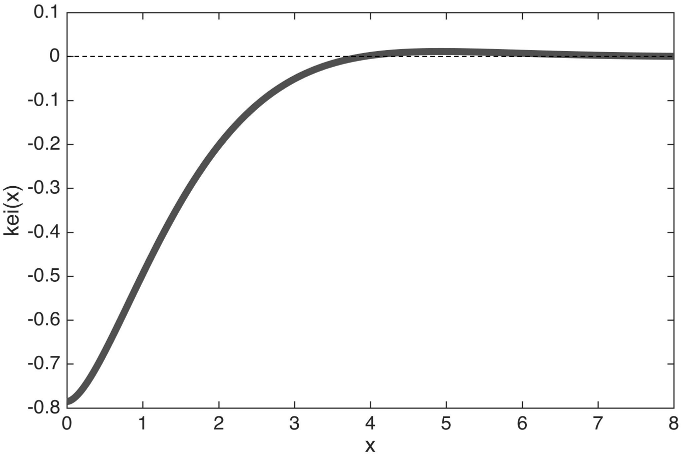

Figure 2.2: Normalised displacement of an arbitrary elastic plate subjected to a point load at $x = 0$. Note the tiny but identifiable bulge at $x = 4$.

If Equation 2.5 is taken with F_0 normalised, it is the fundamental Green's function for a thin elastic plate as shown in Equation 2.7.

$$G(r) = G(x,\check{x},y,\check{y}) = -\frac{L_r^2}{2\pi K_1}\,\mathrm{kei}\left(\frac{r}{L_r}\right) \tag{2.7}$$

The equation above shows the response of a thin elastic plate to a normalised force $F_0 = 1$. In reality however, the force is made up by a large ice sheet. The total deflection at each point can be computed by a summation of all small force elements over the complete area of the ice sheet (Greve and Blatter, 2013). In equation form:

$$w_{ss}(x,y) = \int_{A_{ice}} \rho_i g H_i(x,y)\; G(x,\check{x},y,\check{y})\;\mathrm{d}\check{x}\,\mathrm{d}\check{y}. \tag{2.8}$$

Some assumptions in the elastic lithosphere model are made: It assumes a linear elastic rheology, deflections are assumed to be small with respect to the horizontal plate dimensions, the lithosphere is thin with respect to the horizontal plate dimensions, and planar sections are assumed to remain planar after deflection (Angevine et al., 1990).

2.2.3. Relaxing Asthenosphere Theory

The relaxing asthenosphere model is a method that simplifies the complex dynamics of earth's mantle. In the relaxed asthenosphere analysis the simple decaying function as in Equation 2.9 is used. The adjustment speed of the asthenosphere is dependent on two parts. First, it consist of an inversely proportional constant τ and secondly, the proportional part $(w - w_{ss})$. τ is the relaxation time and $(w - w_{ss})$ indicates the difference between the actual displacement w and the displacement w_{ss} prescribed by the lithospheric model.

$$\frac{\mathrm{d}w}{\mathrm{d}t} = \frac{-1}{\tau}(w - w_{ss}) \tag{2.9}$$

By following the standard differential equation solution, the time dependent solution to equation Equation 2.9 equals:

$$w(t) = w_{ss} + (w_0 - w_{ss})e^{-t/\tau}. \tag{2.10}$$

w_0 is the initial position of the asthenosphere, $w_s s$ the steady state position of the asthenosphere prescribed by the lithosphere response, and w is the actual position at time t. The relaxation time τ solely controls the speed of the exponential decay. Equation 2.10 shows the simplicity of the relaxed asthenosphere model. Its usage is simple and leads to quick computational models compared to other models that try to physically describe the asthenosphere. It is easily implemented in numerical models together with the elastic lithosphere method and the input required is the time constant τ, along with density and elastic parameters (Greve and Blatter, 2013).

However, τ describes in some way the viscosity of the mantle material. The relaxation time is a large simplification of the physical flow behaviour of the asthenosphere that is not definable by one parameter. In reality, different ice sheet sizes cause different relaxation modes due to the complex composition of the asthenosphere (Le Meur and Huybrechts, 1996). This complex behaviour is not supported by the ELRA model.

2.3. Standard Run of the ANICE Model with Eustatic Forcing

In this work, the foundation is the standard run produced by the ANICE model. It is the result of a simulation from -120 000 years to PD with temperature and eustatic sea-level forcing. More importantly, it is computed with a constant relaxation time of 3 000 years (De Boer, 2014). It will serve as a benchmark to which future tests will be compared. In Figure 2.3, the total ice volume is shown for such run. As expected, the volume behaviour is closely related to the temperature and sea level forcing, as shown in Figure 2.1. Note the abrupt change in volume around -15 kyr. This denotes the end of the last glaciation period.

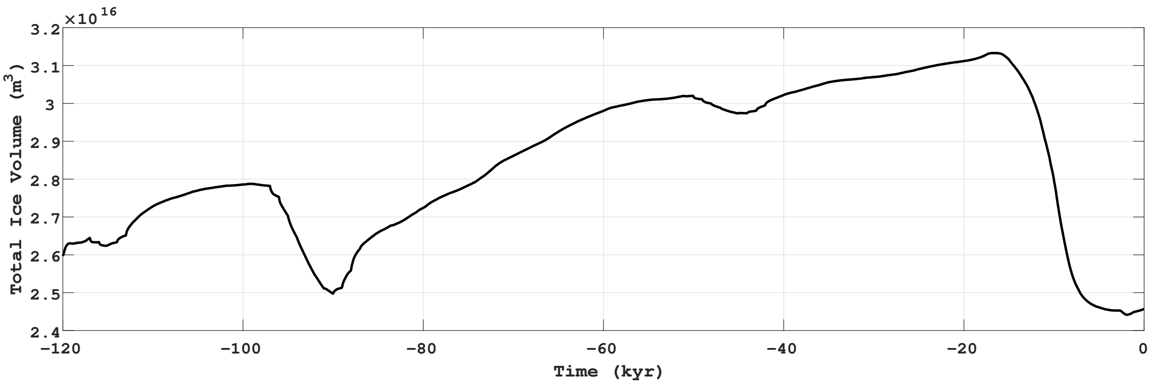

Figure 2.3: Total ice volume for the standard ANICE run for -120 kyr up to PD.

In Figure 2.4 a more detailed view of the last 20 kyr of the base run is presented. In the upper left figure, the ice volume (both total and grounded) is shown over the last 20 kyr. The additional figures show the absolute ice heights in meters of the Antarctic ice sheet development from -20 kyr to PD with incremental 5 kyr steps. In the upper-left figure in Figure 2.4, it can be seen that around -15 kyr a considerable reduction of ice volume starts to take place that notes the end of the last glacial era. The spatial domain in which this happens is focussed mostly on the WAIS. Extensive melt takes place along the Ronne and Ross ice shelves, whereas the east Antarctic ice sheet remains mostly intact. A decrease of 22% in total ice volume is seen from -16 kyr ago to PD.

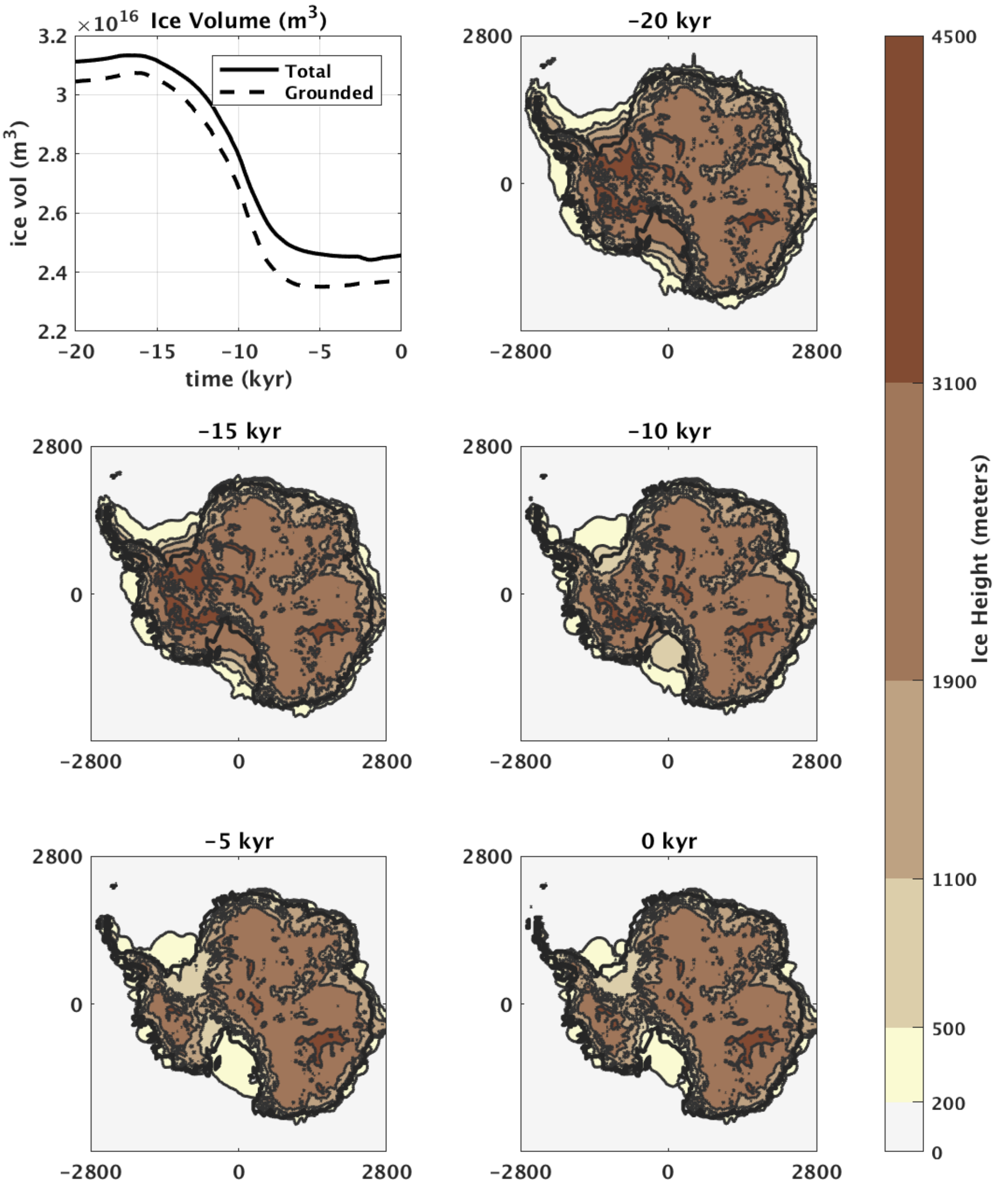

Figure 2.4: The ice height for the standard ANICE model from -20 kyr to PD. The upper left figure shows the total (solid) and grounded (dashed) ice volume. The other five figures show the ice height from -20 kyr to PD with 5 kyr interval.

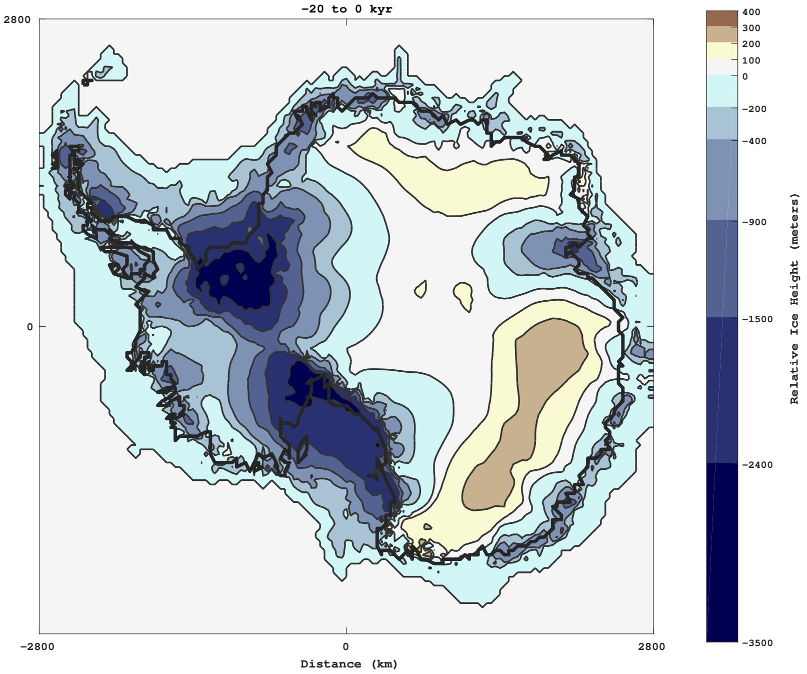

Figure 2.5: Ice height difference between -20 kyr and PD for the standard ANICE run. Large ice mass loss is observed in the WAIS.

Figure 2.5 shows the ice height difference between -20 kyr and PD in a spatial manner. It gives a more detailed insight the ice height decrease along west-Antarctica, where at some places ice height decreases with 3 km over the last 20 000 years. In particular, the Ross and Ronne Ice Shelf show extensive amounts of melt. Furthermore, it is observed that the ice sheet in east-Antarctica is relatively stable, where little ice height growth nor decline can be seen in the central parts of this region. Most ice height decrease at the EAIS is along the ice sheet margins, especially near the Amery ice shelf, which is located in the north-east of the East Antarctic Ice Sheet.

3

The Geoid and ANICE

The stand-alone ANICE simulation presents us with many insights in the behaviour of the Antarctic ice sheet. However, eustatic sea level forcing for Antarctica is not always realistic, as differences occur between the eustatic sea level and the local sea level due to gravitational disturbances and effects induced by other ice sheets in the northern hemisphere. The basic Sea Level Equation (SLE) theory that is needed to understand the implementation is presented in section 3.1. In section 3.3 the implementation of a local sea level surface into the standard ANICE model will be discussed, and the results of this implementation are presented in section 3.4.

3.1. Geodynamics and the SLE

The SLE was first described by Woodward (1888), and Farrell (1973) has described it later in the context of ocean tides. In the context of post glacial adjustment, Farrell and Clark (1976) and Wu and Peltier (1983) described the theory of the SLE. The SLE ”yields the space- and time-dependent change of ocean bathymetry which is required to keep the gravitational potential of the sea surface constant” (Spada and Stocchi, 2007). The SLE is based on the idea that the gravity field of the Earth is not constant, nor perfect. It consists of many irregularities that make the field vary over time and space. These variation are due to density irregularities in the earth’s mantle, which in turn are due to internal and external forces. Furthermore, geographical features such as mountain ridges and deep sea trenches cause anomalies in the gravity field (Fowler, 2011). The theory behind the SLE will be discussed below, as well as the coupling between the SLE and ice sheet dynamics.

The geoid is defined as the shape of the surface of the oceans as if they were under influence of only the Earth’s gravity and rotation. Consequently, the sea level variation is the difference between the geoid height variation and the surface of the underlying solid earth bedrock. The sea level change is a combination of mass interchange by oceans and ice sheets and the solid Earth, shown mathematically in Equation 3.1.

$$S(\omega, t) = \frac{\Phi}{\gamma} - U + c. \tag{3.1}$$

Here, ω is the longitude θ and the latitude λ, and t is time. γ is the gravity acceleration at the surface, Φ is the perturbation in gravitational potential. U is the bedrock vertical displacement and c is a mass conservation function. The geoid surface variation can be written as

$$N(\omega, t) = \frac{\Phi}{\gamma} + c. \tag{3.2}$$

Combining Equation 3.1 and Equation 3.2 leads to the following equation:

$$S(\omega, t) = N(\omega, t) - U(\omega, t). \tag{3.3}$$

Here, S is the sea level variation, N the geoid height variation and U the bedrock height variation. This is the SLE in it's standard form. In Appendix B, the full derivation towards a numerically solvable equation is shown.

The SELEN (SEa Level EquatioN solver) computer program numerically solves the SLE for a non-rotating spherical Earth, that has n layers with Maxwell viscoelastic rheology properties and an inviscid core. It takes the mass distribution of ice I as input, and computes the solid earth response variation U, and the sea surface variation N (Spada and Stocchi, 2007). The SELEN routine will be used in a coupled simulation with ANICE in section 3.3, but first a theoretical background on ice sheet dynamics in combination with the SLE is given.

3.2. The Geoid and Ice Sheet Dynamics

The differences in geoid forcing with respect to eustatic sea level forcing are mainly due to the self gravitation effect of an ice sheet. In Figure 3.1 an schematic overview of differences between the eustatic and geoid sea surface is shown. On the right side of the frame, an ice sheet is shown (white), partially resting on the landmass (brown). The ice shelf is partially submerged in the ocean. The black dashed line shows the eustatic sea level and the black solid line shows the sea surface of the geoid. Due to the large mass of the ice sheet, a gravitational pull is exerted by the ice sheet on the surrounding water. Close to the ice sheet, this results in an increase of sea level. At distances farther away, this gravitational pull becomes weak and sea level is lower with respect to the eustatic sea level.

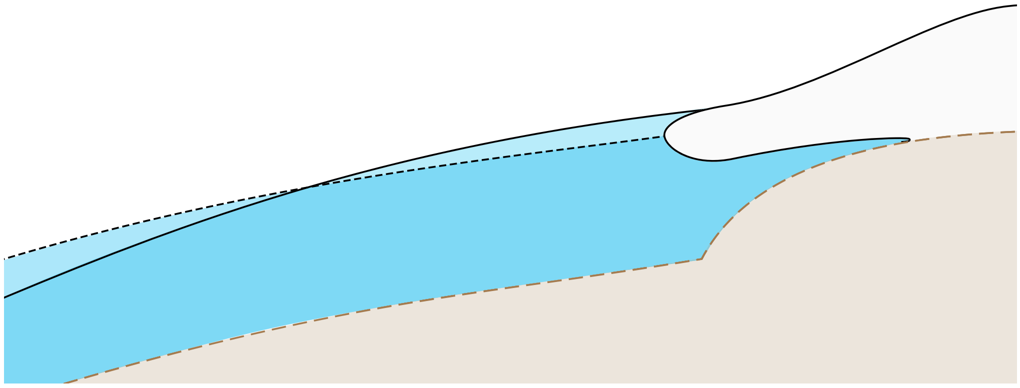

Figure 3.1: Schematic representation of differences between eustatic forcing and using geoid forcing. The ice sheet (white) exerts a gravitational force on the ocean water, which rises relative to the eustatic level close to the ice sheet. At distances farther away from the ice sheet, the sea level falls relative to the eustatic value.

The increase in sea level across the margins of the ice sheet has a stabilising effect on the development of an ice sheet (Weertman, 1974). In theory, one could state that continental bedrock above sea level is beneficial for ice sheet growth compared to ocean surface, as oceans more easily induce melt. Keeping this in mind, when an ice sheet grows, it gains mass, and thus its gravitational pull on surrounding ocean water increases. This increases the sea level along the ice sheet margins, and thus, reduces the rate of growth of the ice sheet. Once an ice sheet melts, its mass decreases. The decrease of mass reduces the gravitational pull of the ice sheet and reduces the sea level along the ice sheet margins. The reduced sea level gives way to continental surface, that maintains the ice sheet (Schoof, 2007).

3.3. the Geoid Sea Surface compared to Eustatic Sea Level

In a basic ANICE run without SELEN, as shown in section 2.3, each ocean point is assigned the same eustatic sea level value. In the previous section it was shown that due to the combination of bedrock variation and ice & ocean loading, disturbances in the gravity field occur. This will cause lateral differences in the sea surface. When ANICE is used in combination with SELEN, there is coupling between the ice sheet, gravity potential of the earth, and the sea level. In this coupled set-up, ANICE computes the ice sheet dynamics of 4 ice sheets (Antarctic Ice Sheet, North American Ice Sheet, Greenland Ice Sheet, European Ice Sheet). For each timestep, the ice sheet loadings are used in SELEN to solve for the response of the earth and the geoid (De Boer, 2014). A coupled SELEN-ANICE run was performed by B. de Boer, where the geoid surface was computed every 1 kyr. The output from this coupled run was the geoid sea surface from -120 000 years to PD. This file was provided by B. de Boer and used in this research.

In Figure 3.2 the sea surface variation from -120 kyr to PD is shown for the eustatic sea level and the provided geoid sea surface. The solid black line represents the eustatic sea level forcing and the red line characterises the sea surface of to the geoid. It is evident that the eustatic sea surface is lower up to ± -16 kyr, which is in agreement with the theory discussed in section 3.2: The ice sheet grows, and sea level drops because of the water-ice conversion. However, mass increase of the ice sheet results in an increase of sea level along the margins of the ice sheet due to gravitational pull. This explains the difference between the two curves in the timeframe from -120 kyr up to -15 kyr. From -15 kyr to PD, a sharp increase in sea level can be observed. Here, it can be seen that the eustatic sea level increases quick compared to the geoid sea surface. Due to the mass loss of the ice sheet, less gravitational pull is exerted on the surrounding water mass, which results in lower sea level. Therefore, the geoid sea surface rises slower compared to the eustatic sea level (De Boer, 2014; Spada et al., 2011). Again, this shows the stabilising nature of the geoid sea surface.

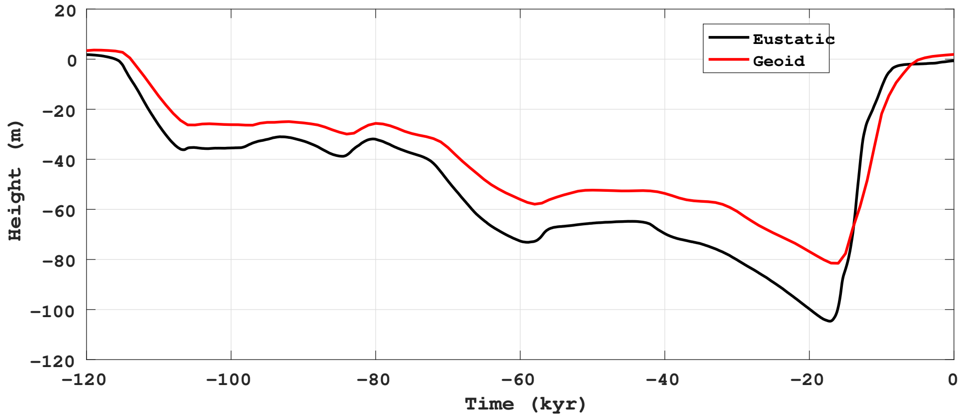

Figure 3.2: Eustatic forcing versus geoid forcing w.r.t PD. The red line presents the mean geoid height along the Antarctic region. The solid black line presents the previously used eustatic forcing.

3.4. Implementing the Uncoupled Geoid in ANICE

The ANICE model is altered in such way that it uses the provided geoid sea surface forcing instead of the eustatic sea level forcing. It should be noted that this implementation is not a coupled implementation of any kind. There is no interaction between the dynamic ANICE ice model and the geoid sea surface input file. Changes in bedrock and/or ice sheet height do not alter the geoid surface. It is assumed that the theoretical geoid sea surface from any future run does not deviate strongly from the computed sea surface from the coupled SELEN-ANICE run.

The provided geoid sea surface is used as sea level forcing in a simulation to replace the eustatic sea level forcing. The ANICE routine was altered to allow for this modification. The geoid values are interpolated every 100 year to prevent step-wise behaviour on larger time-scales. In Appendix B the modified FORTRAN code that implements the geoid sea surface into the standard ANICE model is discussed.

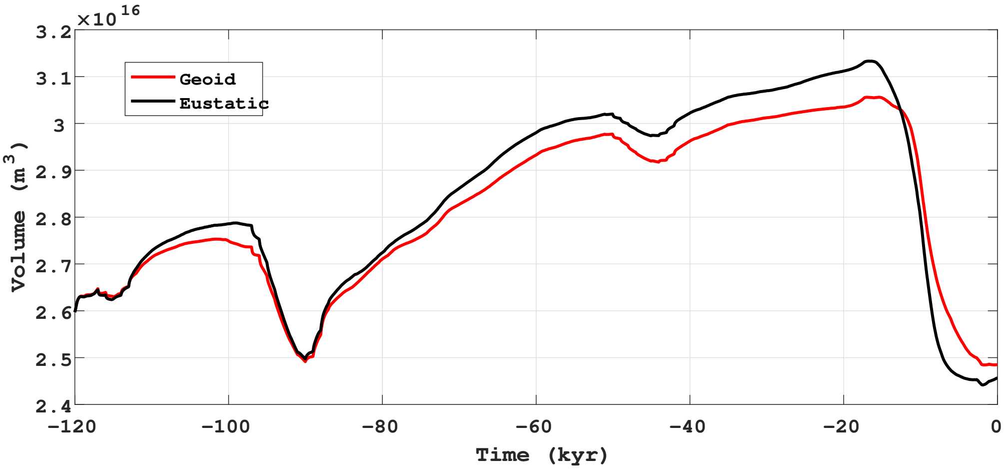

Figure 3.3: The ice volume for the the model with geoid forcing in red. The black curve represents the ice volume for the model with eustatic forcing.

Figure 3.3 shows the ice volume development of the geoid forced model (red) and the eustatic sea level forced model (black). It can be seen that the patterns follow a similar but inverted trend with respect to the sea surfaces in Figure 3.2. Observed in Figure 3.3 is a smaller ice volume for the geoid model during the build up phase from -120 kyr to -15 kyr. From -15 kyr to PD, the ice volume for the geoid model is larger compared to the eustatic model. Ice volume difference at LGM is 8.5·10^{14} m^3, (SLEQ 2.1 m). At present day the difference is 2.9·10^{14} m^3 (SLEQ 0.8 m).

Figure 3.4 shows the difference in ice height between the eustatic run and the geoid run for 5 points in time. A positive value implies a larger ice height in the eustatic run. A notably larger ice height is observed for the eustatic model in the period from -20 to around -15 kyr. Here, the eustatic run shows larger quantities of ice mostly in the region of the Ronne and Ross ice shelf. At -10 kyr and -5 kyr, a change can be seen where the ice height in the eustatic run becomes smaller. This is mostly seen in the same regions. The observed differences can be explained by the aforementioned theory of the stabilising effect of the geoid. Whereas the eustatic sea level uprise is relatively abrupt and induces a lot of melt at the ice sheet margins, the geoid sea level rises in a relatively slow manner, due to the reduced gravitational pull of the ice sheet. This results in less ice sheet melt, and thus a relatively larger ice sheet at PD compared to the eustatic model.

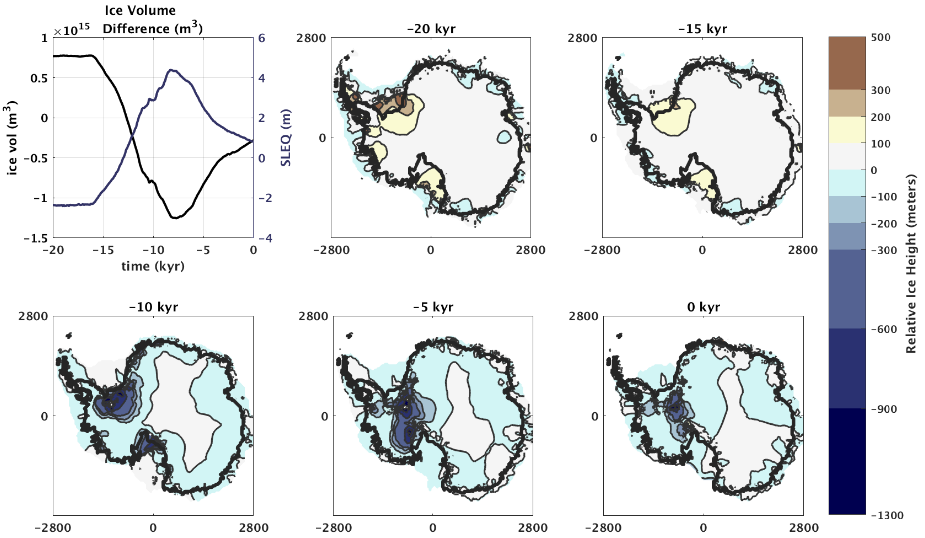

Figure 3.4: Absolute ice height differences between the eustatic and geoid forcing at five points in time. The values are obtained by subtracting the geoid model ice height values from the eustatic model ice height values.

The geoid sea surface model provides more accurate sea levels along the margins of the ice sheet compared to eustatic sea level, mainly due to self-gravitation of the ice sheet (de Boer et al., 2017; Spada et al., 2011). Therefore, the geoid sea surface forcing will be used in future simulations with laterally varying relaxation times. The aim is to accurately simulate the complex bedrock uplift and sea level relationship at the ice sheet margins of the WAIS.

4

Using Viscosity Data to Model Ice Sheet Development

In this chapter the focus will change to the bedrock adjustment by the ELRA model. The ELRA routine in ANICE requires relaxation time as input. However, available bedrock property data is in the form of viscosity values for separate layers in earth's mantle. First, the theory of the solid earth will be discussed in section 4.1. Different viscosity models are presented in section 4.2. The conversion of these viscosity models to relaxation time will be discussed in section 4.3. The chapter is concluded by the ANICE implementation of wavelength dependent relaxation time in section 4.4.

4.1. Theory of the Solid Earth

The earth can be divided into mechanical layers dependent on the stiffness of the layers. The top layer is the lithosphere, and consists of the crust and the upper part of the mantle. The lithosphere behaves brittle on small timescales and elastically on timescales of in the order of thousand of years (Greve and Blatter, 2013). The oceanic lithosphere thickness varies between 50 and 140 km whereas the continental lithosphere thickness varies between 40 and 240 km (Pasyanos, 2010). The asthenosphere is the layer underneath the lithosphere. The boundary between these two layers is taken at the 1300 K isotherm (Artemieva and Mooney, 2001). The asthenosphere extends to a depth of 700 km. The asthenosphere behaves viscoelastic - it has elastic and viscous properties. The property that has most influence on the time-dependent loading-response of the asthenosphere is the viscosity parameter. In GIA modelling, the mantle's rheological behaviour is usually described by homogeneous layers of different viscosity (Kaufmann and Lambeck, 2002; Peltier, 2004).

However, lateral and radial variations of viscosity occur throughout the earth's interior (Goes et al., 2000; Ivins and Sammis, 1995). The depth dependency of viscosity is closely related to increasing pressure and temperature in deeper mantle layers (Bunge et al., 1996). Lateral variations in viscosity occur mostly due to chemical and thermal anomalies in mantle composition (Forte et al., 1995; Jordan, 1978). Moreover, in Antarctica, seismic wave velocities indicate a strong variation in bedrock properties between East and West Antarctica (An et al., 2015; Heeszel et al., 2016; Kaufmann et al., 2005; Morelli and Danesi, 2004). When focussing on lateral and radial viscosity dependency with respect to ice sheet behaviour, five regions in Antarctica can be identified that are significant. Note that those regions are not necessarily interesting solely for their mantle properties or ice sheet behaviour, it is the combination of these two factors that might lead to interesting results (Groh et al., 2012; Nield et al., 2014; van der Wal et al., 2015; Whitehouse et al., 2012, 2017a). In Figure 4.1 the five regions are shown:

1. Ronne Ice Shelf (referred to as Ronne)
2. Ross Ice Shelf (Ross)
3. North Antarctic Peninsula (NAP)
4. East Antarctic Ice Sheet (EAIS)
5. Amundsen Sea Sector (Amundsen)

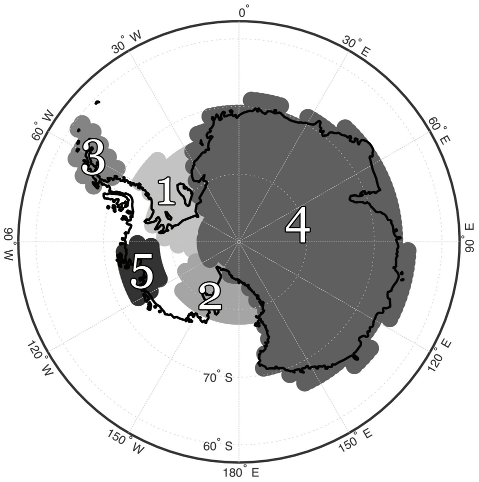

Figure 4.1: Antarctica regions that show significant properties for ice sheet dynamics with respect to viscosity differences.

Region 1 and 2 are the Ronnne and Ross Ice Shelves. In section 2.3 it was shown that in these two regions, most melt occurs during the last melt epoch. This automatically makes those regions interesting to focus on. Region 3 is the North Antarctic Peninsula, that has very low predicted values for viscosity, together with the Amundsen Sea Sector (region 5). The EAIS (region 4) on the other hand has expected viscosity values that are significantly higher and therefore this region has a completely different feedback compared to the other four regions.

Figure 4.2 shows the viscosity values for the Antarctic region for depths of 52, 95, 145 and 200 km using the SLHE10W viscosity model. For small depths, the strength of the lithosphere dominates and viscosity values are high. Deeper layers show a complex variation of viscosity that strongly varies laterally. One considerable property is the high viscosity for the EAIS region, and the abrupt change to low viscosity in the WAIS region. This change is not only lateral, but also depth dependent, as seen in Figure 4.2.

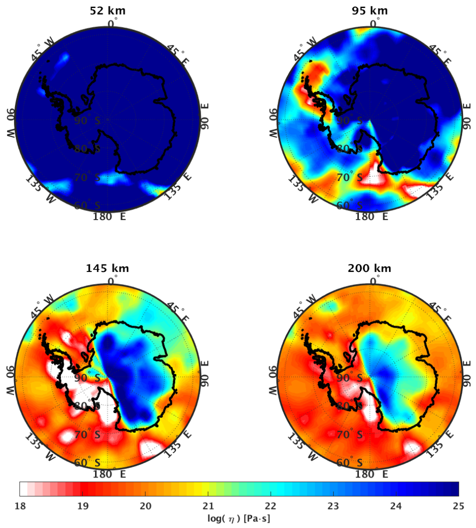

Figure 4.2: Viscosity values for 4 different depths using the SLHE10W model. From van der Wal et al. (2015).

4.2. Viscosity Models for Antarctica

Viscosity data for the Antarctic region as shown in Figure 4.2 is derived from seismic wave velocity models. Such seismic waves models exist for the complete earth, but regional models exist as well. A global seismic wave model is the Schaeffer and Lebedev (SL) model. It is a global seismic wave model for upper mantle shear speeds by Schaeffer and Lebedev (2013) based on tomography. Next to that, the Heeszel (HE) model contains local seismic data for Antarctica (Heeszel et al., 2016). The combination of the global HE model and the local HE model results in the SLHE (Schaeffer and Lebedev - Heeszel) model, which is created by Dr. P. Whitehouse[1] and provided for this research.

4.2.1. Viscosity From Seismic Data using a 3D FEM Model

In this section, a method for converting seismic wave models to viscosity maps is discussed. Equation 4.1 shows the equation for the effective viscosity (Van Der Wal et al., 2013):

$$\eta_{eff} = \frac{1}{3B_{diff} + 3B_{disl}q^{n-1}}. \tag{4.1}$$

In this equation, η_{eff} is the effective viscosity, B_{diff} and B_{disl} are the diffusive and dislocation creep, q is the von Mises stress and n is stress. The creep B can be approximated by (Hirth and Kohlstedt, 2003):

$$B = Ad^{-p} fH_2O^r e^{\alpha\varphi} e^{-\frac{E+PV}{RT}} \tag{4.2}$$

where A and α are constants, d the grain size, fH_2O the water content, E the activation energy and V the activiation volume, P the pressure and R the gas constant. T is temperature, p and r are the grain size and water fugacity exponents, respectiviely. In this equation, E, V, p, r and A are taken from Hirth and Kohlstedt (2003) for each respective creep model. Pressure is a function of depth and is assumed to have a gradient of 0.033 GPa/km (Kearey et al., 2009). The melt content φ is equal to zero. It was shown by Barnhoorn et al. (2011) that melt content has little influence relative to grain size and water content. The temperature T is derived from the respective seismic models.

---

[1] Dr. P. Whitehouse, Department of Geography, Durham University

The seismic data is converted to temperature using the depth-dependent temperature derivative used for seismic wave velocities (Karato, 2008). In this conversion the assumption is made that all seismic perturbations are of thermal nature, and chemical perturbations are neglected. This assumption is valid according to Cammarano et al. (2011), who states that chemical perturbations are probably small compared to thermal perturbations in upper mantle layers. However, it should be noted that according to Wu et al. (2013), these assumptions can influence GIA predictions. In order to compute the effective viscosity, a finite element model is used. a FEM analysis is required because the problem becomes non-linear due to the fact that in Equation 4.1, effective viscosity is dependent on stress. This implies that effective viscosity is dependent on the ice loading in case of GIA.

The finite element model used in van der Wal et al. (2015) has 2° x 2° spatial elements and 8 vertical layers. The model is self-gravitating and deformation is computed through two types of creep: deformation creep and dislocation creep. The upper layer (0 km - 35 km) behaves purely elastic. Other layers are assumed to be viscoelastic. At depths above 400 km, the flow laws of Hirth and Kohlstedt (2003) are used to compute the creep as in Equation 4.2. In a study by van der Wal et al. (2015), models with different water content (wet: 1000 ppm H_2O, dry: 0 ppm H_2O), grain size (1, 4, 10 mm), and seismic data was used. The performance of the resulting viscosity model was checked by loading and unloading 2 non-dynamic ice histories and comparing the model bedrock deflection to uplift data in Scandinavia and North America. A selection of models was made were the simulated uplift was in best agreement with uplift measurements in the northern hemisphere.

The seismic model with the best uplift fit was a model with 4 mm grain size and dry rheology. The best fit with relative sea level in Fennoscandia was a model with 10 mm grain size and wet olivine. The proposed grain sizes of 4 mm and 10 mm however do not comply with xenoliths found at Antarctic locations. At several of these locations found xenoliths had grain sizes in the range of sub-millimetre to a few millimetres both with high and low water content (van der Wal et al., 2015). The combination of those findings resulted in the following preferred viscosity models: SL 4D, SLHE 4D, SLHE 10W, and SLHE 1D[2].

It is imperative to consider the differences in these models in order to explain differences in model outputs. As shown in Equation 4.2, effective viscosity is dependent on grain size and water content. Combining Equation 4.1 and Equation 4.2 leads to the simple approximation that an increase in grain size leads to higher viscosity values, and and increase in water content leads to lower viscosity values, if other parameters are kept constant.

4.3. Converting Viscosities to Relaxation Time

There is no straightforward method for converting viscosity maps to relaxation time maps. The laterally and radially varying viscosity underneath Antarctica produces a complex rebound signal, which is not easily confined in one single relaxation time. The complex bedrock uplift can be defined as a combination of several modes that each produce a different rebound signal (McConnell Jr, 1965; Spada et al., 2011). Generally speaking, different uplift modes are excited by large surface loadings, and the dominant uplift mode that is excited depends on the wavelength of the surface loading. From

---

[2] The notation is as follows: **SLHE**/**SL**: seismic model, **10**/**4**/**1**: grain size (in mm), **W**et/**D**ry: water content

the dominant uplift mode, an approximation of the dominant relaxation time can be made (Whitehouse et al., 2017b).

The following procedure is used to convert each layered viscosity map to a relaxation time: initially, a normal mode model is used to convert, for each region as in Figure 4.1, the complex viscosity layering to a bedrock relaxation curve for a number of different ice cap loadings. In this model, the ice cap wavelength is varied to excite different uplift modes. Hereafter, the resulting bedrock uplift curves are fit to a purely exponential curve to identify the dominant uplift mode, which results in a relaxation time.

In short, the following is done to convert the complex viscosity field to a relaxation time, for each of the five regions:

1. Compute the average viscosity for each depth at the specific region, for the given viscosity model.
2. Assign the computed values from 1) to the five layers of the normal mode model.
3. Simulate surface displacement curves by loading the layered normal mode model using ice cap loading with varying wavelengths.
4. Fit the complex displacement curves to a purely exponential curve and determine the relaxation time, for each ice cap wavelength.

4.3.1. Creating Displacement Curves using a Normal Mode Model

The normal mode consist of five layers and simulates bedrock deflection over time based on the loading of the model. The basic set-up of the normal mode model used here consists of forcing the model with a certain loading, and after equilibrium is reached, this load is removed. The displacement is computed from $t = 0$ (equilibrium load removal) up to 15 kyr. This simulation is done for several ice loadings, where the wavelength varies from 0.625° to 10° (Whitehouse et al., 2017b). The simulations were done by dr. ir. W. van der Wal[3] and provided for this research.

Table 4.1: average $\log_{10}$ viscosities for the SLHE4D model.

Depth (km)	Ronne	Ross	NAP	EAIS	Amundsen
52	50.2	49.0	29.1	48.5	35.7
95	30.6	27.5	23.1	29.9	24.3
145	23.4	20.7	21.0	26.5	20.5
200	21.8	20.2	21.1	24.4	20.4
315	20.6	20.2	21.6	21.2	20.1

For each viscosity model and for each region as in Figure 4.1, the average viscosity value per depth is determined. For the SLHE 4D model, these average viscosity values are shown in Table 4.1. Consequently, for each viscosity model, the normal mode model is run twenty-five times: five different

---

[3] Dr. Ir. W. van der Wal, Faculty of Aerospace Engineering, TU Delft

regions, and five different wavelengths per region (0.625°, 1.25°, 2.5°, 5° and 10°). Each run results in one uplift curve. In Figure 4.3 (a) five uplift curves produced by the normal mode model are shown, for the SLHE4D model at the Ronne location. Same for Figure 4.3 (b), where the Ross region uplift curves are shown. These curves are computed for the 3 other regions too, as well as for all other viscosity models. It can be seen that for a larger wavelength of the ice cap, the initial deflection is also larger. The uplift shows semi-exponential behaviour: not all curves do converge to zero and some curves intersect, showing a complex uplift signal.

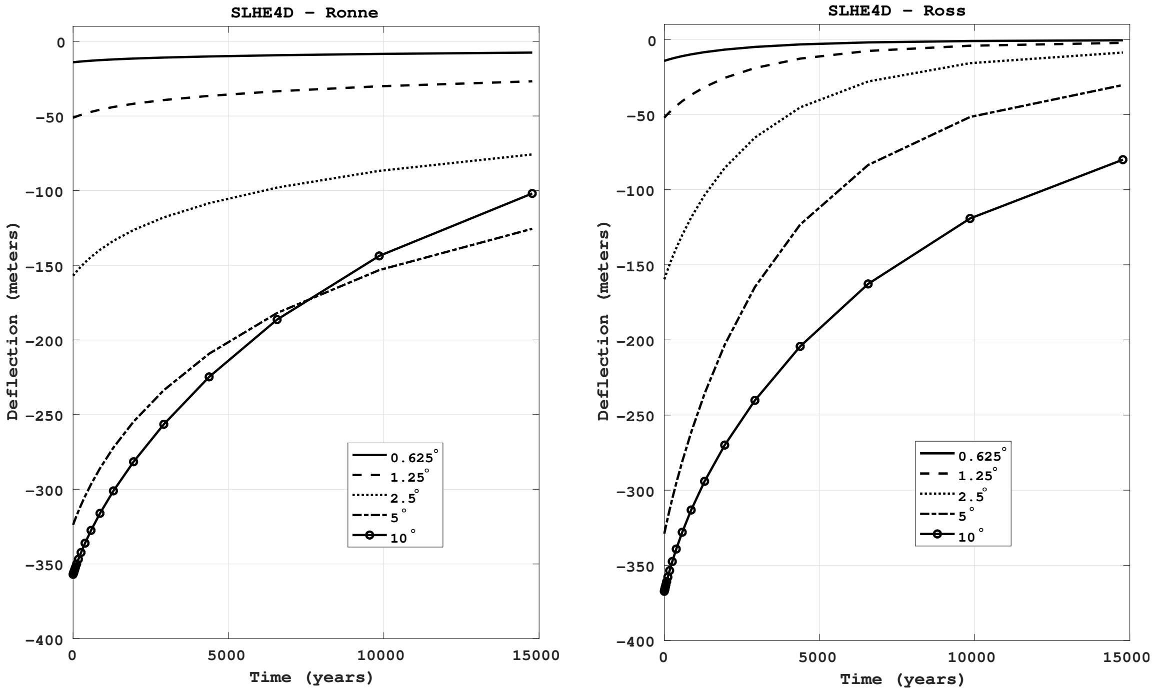

(a) (b)

Figure 4.3: Uplift curves for the Ronne (a) and Ross (b) region for the SLHE4D viscosity model. 5 different wavelengths are used for the bedrock loading.

4.3.2. Fitting Bedrock Displacement Curves to an Exponential Curve

Next, each displacement curve must be fit to an exponential to obtain a relaxation time. Matching the displacement to a relaxation time is done through curve fitting a purely exponential curve to the displacement curve from the normal mode model, of which ten are shown in Figure 4.3a & b. The normal mode displacement curve has, besides its purely exponential signal, many disturbances. For example, the displacement curve can consist of a fast rebound mode from one layer, and a slow rebound mode from a different, more viscous, layer. To account for this inconsistency, the slow rebound signal is removed from the curve and the exponential curve is fitted solely to the fast - in the order of hundred to thousand years - signal. It was chosen to discard the slow rebound signal because these are less significant, especially in the last melt epoch. Slow rebound signals in the order of 20000 years or more have little effect in this era, as most effects occur on much smaller timescales, where the a fast rebound signal is more influential.

In Equation 4.3 the simple exponential equation to which the displacement curves is fitted is shown. The first term contains the relaxation time in the exponential function, and the second term, b, compensates for the slow rebound signal.

$$h(t) = exp(t/\tau) + b. \tag{4.3}$$

In Figure 4.4 the normal mode displacement curve (solid) is shown, as well as the exponential fit (dashed). The exponential fit has a relaxation time τ of 4500 years, and a correction term $b = 130$. It can be seen that the normal mode displacement starts exponentially, but around ± 5000 years the exponential curve starts to behave less exponential and the curves diverge. The effective relaxation time obtained by this method is an approximation of the complex viscosity layering used in the normal mode model (Whitehouse et al., 2017b). A more in depth discussion of this method is found in Appendix C.

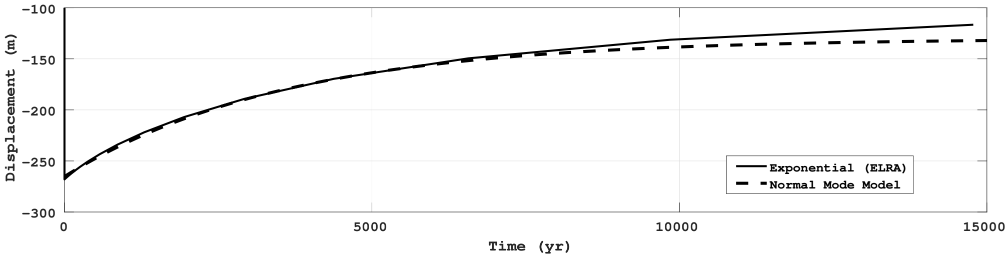

Figure 4.4: Exponential fit (dashed) on the normal mode displacement (solid) of the NAP location for the SLHE 4D model. The correction term b is 130 meter.

Below, in Table 4.2 up to Table 4.6, the determined relaxation times per wavelength are shown for each region. Note that for the EAIS in Table 4.6, where no variation between models was expected, only the SLHE4D model was converted from viscosity to relaxation time.

Table 4.2: Relaxation times for the Ross region.

Size (deg)	SLHE10W	SLHE4D	SLHE1D	SL4D
0.625	120	3300	90	2300
1.25	300	3300	110	1400
2.5	500	3200	75	1700
5.0	900	4500	300	2600
10.0	2300	6000	900	6100

Table 4.3: Relaxation times in years for the Ronne region.

Size (deg)	SLHE10W	SLHE4D	SLHE1D	SL4D
0.625	2400	3800	800	4600
1.25	2800	3800	1500	4250
2.5	3200	4000	1500	4100
5.0	7600	6100	1800	5300
10.0	20000	5800	3600	5700

Table 4.4: Relaxation times in years for the Amundsen region.

Size (deg)	SLHE10W	SLHE4D	SLHE1D	SL4D
0.625	200	1700	30	900
1.25	200	1900	40	1100
2.5	400	2000	75	1300
5.0	900	2800	150	2200
10.0	2200	5800	800	5200

Table 4.5: Relaxation times in years for the NAP region.

Size (deg)	SLHE10W	SLHE4D	SLHE1D	SL4D
0.625	1000	4000	800	2300
1.25	1200	3500	400	3100
2.5	2400	4500	400	3900
5.0	6200	7000	600	5000
10.0	16000	7200	1550	5250

Table 4.6: Relaxation times in years for the EAIS region.

Size (deg)	SLHE4D
0.625	4500
1.25	6000
2.5	12000
5.0	22000
10.0	22500

4.4. Implementing Laterally Varying Relaxation Time into ANICE

The ANICE model, and specifically the ELRA module must be modified to work with this method of relaxation time input. The module has the ability to use spatially varying relaxation times, as this was already implemented in the model by Pablo Vizcaino Rubio. However, in this case it is also desired that the ELRA module computes the ice cap wavelength in each of the specific regions. To do so, the ELRA module is extended in such way that it determines the wavelength of the ice cap in each region on runtime. Next, the details of this extension is discussed. For a more in-depth discussion, as well as the corresponding Fortran code, the reader is referred to Appendix D.

The following method is added to the ANICE bedrock module. This bedrock module is used with a 100 year timestep. Each time the bedrock module is called, the ice sheet wavelength is computed for each location.

It is assumed that the bedrock is fully adjusted to the ice thickness at the start of the run, at -120 kyr. Therefore, the ice thickness used for determining the ice sheet wavelength is reduced by the ice already adjusted for in the far past; this is done by subtracting the ice height at -120 kyr from the current ice height. Points that have negative ice height after this subtraction, are discarded from the analysis. Naturally, points outside the region and ungrounded points are also not considered. Lastly, a filter is applied to exclude isolated ice grid points from the analysis.

The ice sheet wavelength is consequently determined by computing the largest distance between the remaining ice points in the region. The determined wavelength will be used in order to obtain a relaxation time. If the determined wavelength lies within the range of 0.625° - 10°, the relaxation time will follow from simple interpolation. If the determined wavelength is below 0.625°, the relaxation time is set to the value associated with 0.625°. The same holds for a determined wavelength larger than 10°. In such case, the determined wavelength is capped to 10° and so is the relaxation time.

The regions that do not lay directly into one of the five predetermined regions are averaged, taking surrounding regions in mind. This approach results in the full relaxation time grid to be filled with relaxation values in agreement with the wavelength of the ice sheet above it. A smoothing algorithm is used to apply a smoothing of the relaxation time values between the boundaries of the regions. In the original viscosity data, there is a 200-300 km viscosity transition region between for example, east and west Antartica (van der Wal et al., 2015). The smoothing algorithm takes the mean value of a number of grid points creating a smooth transition region of ±280 km for all region boundaries.

5

ANICE Results of Several Viscosity Models

In this chapter the results of the ANICE runs with the SL4D, SLHE4D, SLHE10W and SLHE1D models will be discussed. First, the adaptive relaxation time module results are being presented in section 5.1. The differences in the four different models with respect to each other and the benchmark model will be discussed in section 5.2. In this section, several regions will be discussed more thoroughly because of their compelling melt behaviour. In concluding section 5.3, a sensitivity test is shown to give an indications on the significance of the results.

5.1. Adaptive Relaxation Time Module Results

As presented in the previous chapter, the relaxation time is dependent on the wavelength of the ice loading at the surface. The performance of the wavelength determination module will be presented in this section. In this section the focus will mainly lie on the last melt epoch, as here most changes occur and thus adaptive relaxation time is best visible.

In Figure 5.1, the ice cap wavelength for the predetermined regions are shown for three points in time. The grey area defines the ice surface that remains after subtracting the reference ice height, as discussed in section 4.4. The solid black line indicates the largest distance within the remaining points, after filtering for isolated points. Here, the EAIS wavelength is not shown, as it does not show variability. At -15 kyr, all regions have maximum wavelength. The Ronne region has the largest wavelength (7.6°) and the NAP region the smallest wavelength (2.8°). The center figure shows the wavelengths at -10 kyr. A reduction for the Ross region and the NAP region can be observed: the Ross region wavelength reduces by 40% and the NAP wavelength reduces to 0.18°. Wavelengths in the Amundsen and Ronne regions stay nearly the same. At the next epoch (-5 kyr), the wavelengths for the Amundsen and Ronne region decrease as well. The Ronne region decreases largely in ice sheet surface, however the wavelength reduction is small. This effect will be further discussed in section 6.3. The wavelength for the Amundsen region decreases by 16% and the Ross ice sheet wavelength decreases by 58%.

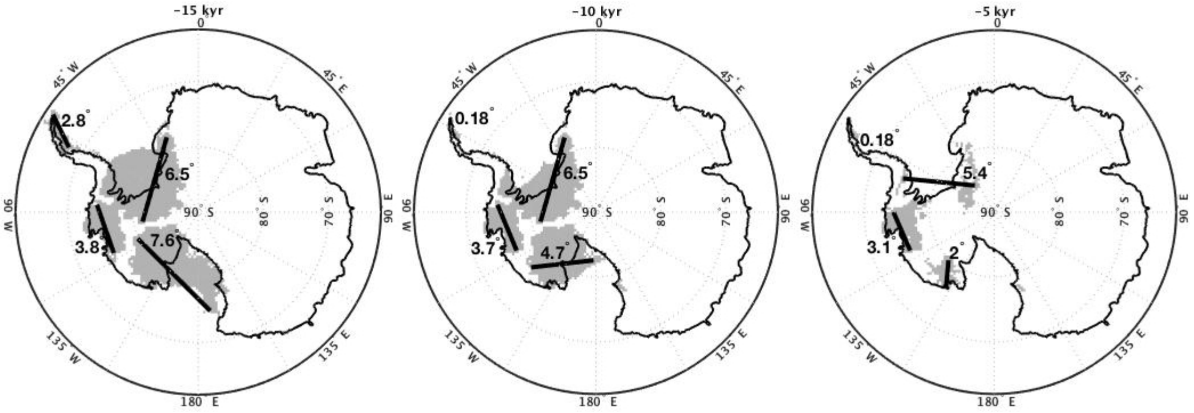

Figure 5.1: Wavelength of several regions for three different points in time. Model used: SLHE4D.

Figure 5.2a shows the determined wavelength during runtime in the Ross region for each model. Figure 5.2b shows the relaxation time that follows from the determined wavelength in combination with the determined relaxation times in the previous chapter. Figure 5.2a shows a decreasing pattern for all models. A big drop in wavelength occurs for all models at -10 kyr, which is also observed in the Ross region in Figure 5.1. The SLHE4D model shows a second drop around -7 kyr. The results of the wavelength drop at -10 kyr can be seen in the right figure, where the relaxation time drops for each model. For the SLHE4D curve a second drop occurs around -7 kyr, which is in agreement with the reduction in wavelength around this time, as seen in the left graph.

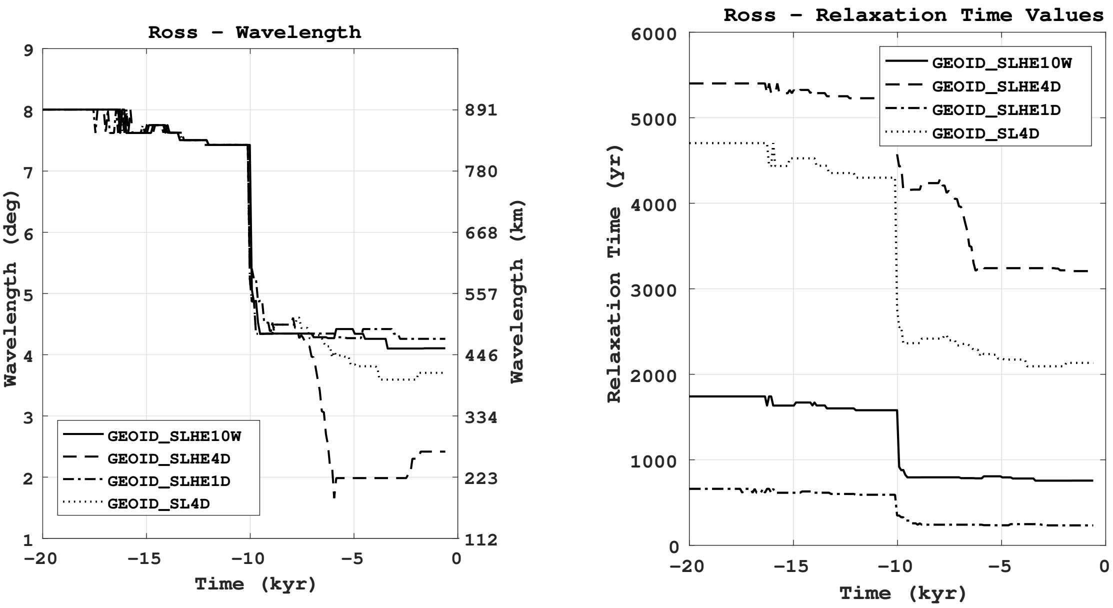

(a) (b)

Figure 5.2: The wavelength (a) and relaxation time (b) for the Ross region from -20 kyr to PD.

Figure 5.3a shows the determined wavelength during runtime in the NAP region for each model. Figure 5.3b shows the relaxation time that follows from the determined wavelength in combination with the determined relaxation times in the previous chapter. Here slightly different results are seen compared to the Ross region. All wavelength curves shows a steady decrease from 3.2° to 0.18°, which is the minimum wavelength set in the adaptive relaxation time method. Unlike the Ross region, where decreasing wavelength resulted in decreasing relaxation time, the NAP region shows an increase in relaxation time for some models. Specifically, the SLHE4D and SLHE1D model show increasing relaxation time with decreasing wavelength. Referring back to Table 4.5, it can indeed be seen that those models show non-linear behaviour for smaller wavelengths at the NAP location.

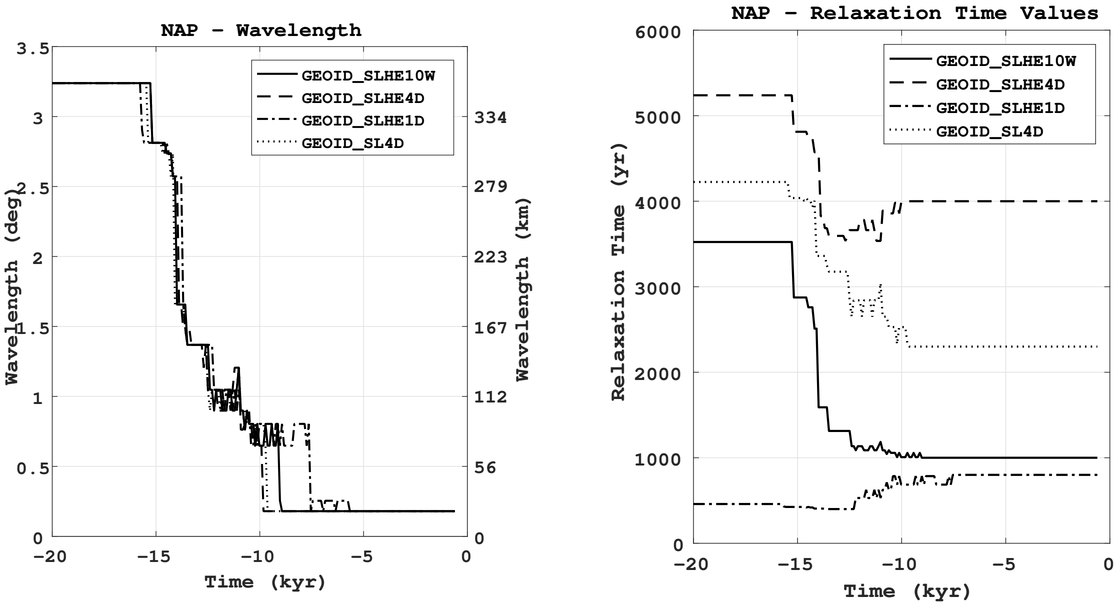

(a) (b)

Figure 5.3: The wavelength (a) and relaxation time (b) for the NAP region from -20 kyr to PD.

5.2. Ice Volume & Bedrock Uplift Results

In Figure 5.4 the ice volume development of the four laterally varying relaxation time models is shown, together with the benchmark model. The red line shows the benchmark model that has a constant relaxation time of 3000 years. The solid black curve is the SLHE10W model, dashed is SLHE4D, dot-dashed is SLHE1D, and the SL4D model is the dotted curve. It is observed that the benchmark model has a smaller total ice volume during a large part of the period. In the last 20 kyr this becomes less apparent. In Figure 5.5 this epoch is shown in more detail. It can be seen that after LGM, where the ice volumes are very close, the ice volumes of the different models start differentiating. Around -10 kyr, differences start to grow between the different models. The ice volume differences expand up to PD.

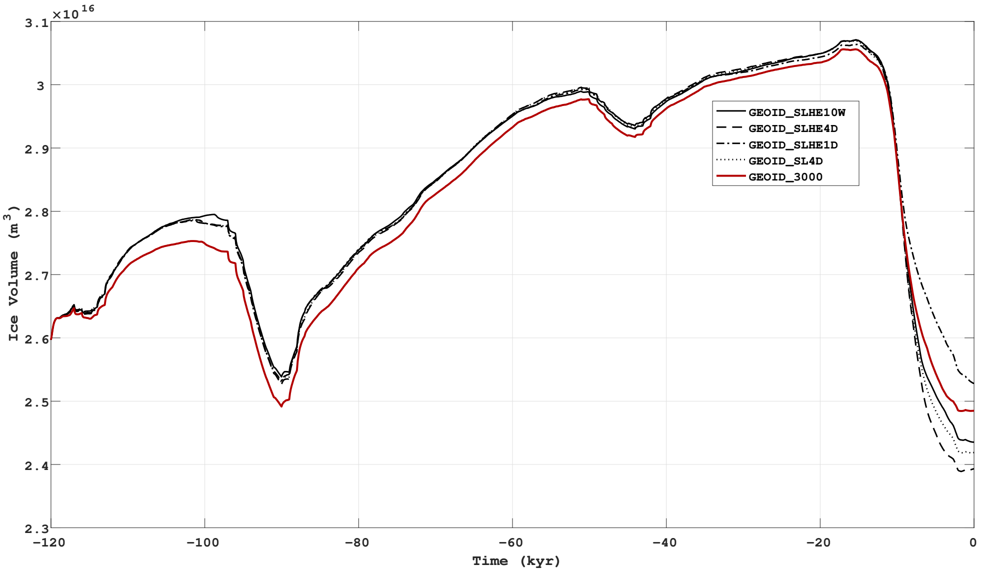

Figure 5.4: Total ice volume development for 5 different models for the -120 kyr to PD timeframe.

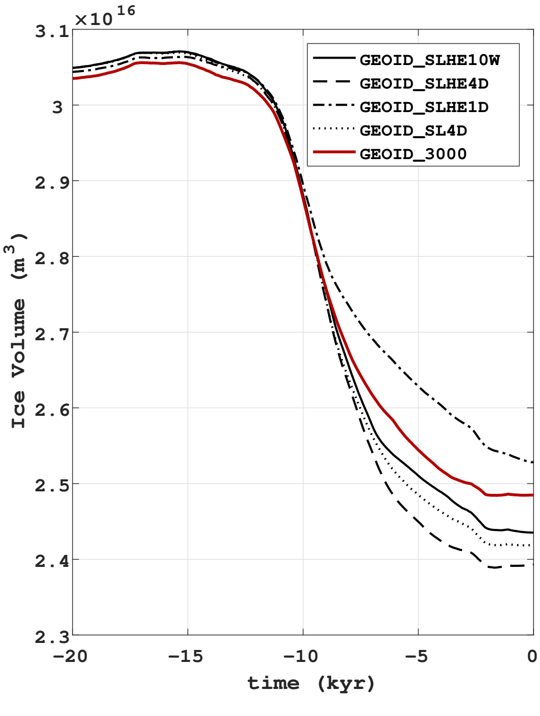

Figure 5.5: Ice volume development for 5 different models for the -20 kyr to PD timeframe.

The observed differences in the timeframe from LGM to PD are shown in Table 5.1. The metric LGM - PD was chosen because at LGM the ice volumes are mostly converged and there are only minor differences between the models. Moreover, the observed differences at LGM are small compared to the differences observed at PD.

Table 5.1: Ice volumes at LGM and PD for different models.

Model Name	**LGM** $(10^{16}\ \mathrm{m}^3)$	**PD** $(10^{16}\ \mathrm{m}^3)$	**%**
GE3000	3.133	2.485	-20.58
SLHE4D	3.069	2.393	-22.03
SLHE10W	3.069	2.435	-20.66
SLHE1D	3.062	2.528	-17.44
SL4D	3.068	2.419	-21.19

Notable differences are observed between the four models and the benchmark model. The SLHE1D model most certain has the smallest ice volume decrease (17.44%), whereas the SLHE4D model shows the largest decline in ice volume (22.03%). The SL4D and SLHE10W models show most agreement with the benchmark model, for the -20 kyr to PD melt epoch.

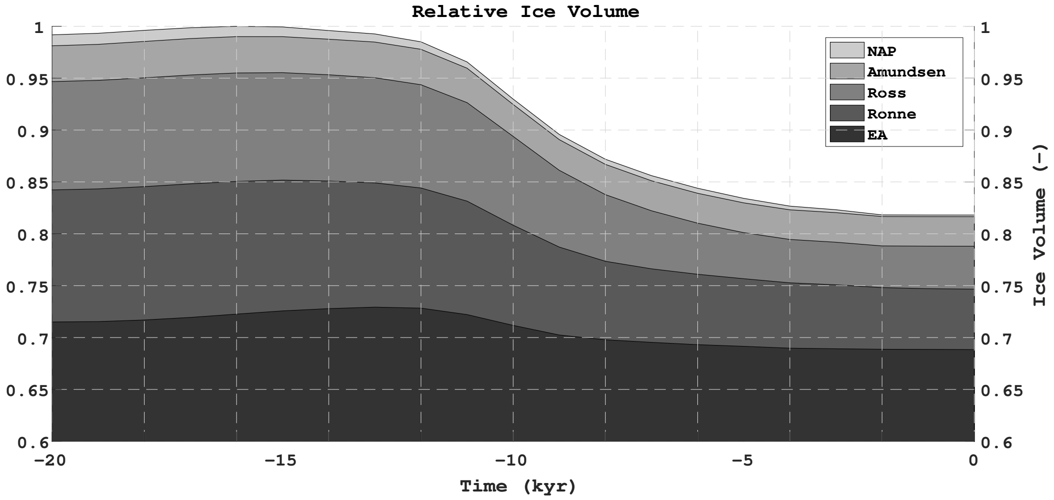

Figure 5.6: Stacked normalized ice volume curves present a clear view of in which regions most melt occur during the -20 kyr to PD melt epoch. From dark grey to light gray: East Antarctica, Ronne, Ross, Amundsen, NAP. Note that the y-axis starts at 0.6.

In Figure 5.6 the normalised ice volume per region over the period -20 kyr to PD is shown. It can be easily observed that the largest melt contributions are from the Ross and Ronne regions. The Amundsen region mass loss is smaller than the Ronne and Ross region. Although the NAP has a very large percentage decrease in ice volume, the absolute ice volume decline in this region is relatively small. The relative mass loss in East Antarctica is small as well. That is why in the next section, the Ross and Ronne region are the primary focus.

5.2.1. Bedrock Uplift in Antarctic Regions

In this section, results of bedrock uplift is shown. Specifically, the focus will be on the Ross and Ronne regions. These two regions are subject to the largest ice volume decrease. Here, the choice is made to present bedrock data for regions along the ice sheet margin that become unloaded after LGM. In other words, those points have grounded ice at LGM, but after LGM the ice sheet retracts and the bedrock is unloaded. As a result, the uplift is much less constrained by ice loading and results provide more insight in uplift scenarios.

Bedrock Uplift in the Ross Region

Here, a more in-depth analysis of the uplift in the Ross region will be given. In Figure 5.7 the location where bedrock will be analysed is shown by the circle. At this location, at LGM, the ice is grounded, but once the melt episode starts, ice will be floating due to grounding line migration. The B-B' line indicates the position that is shown in the bedrock - ice shelf interaction in Figure 5.8.

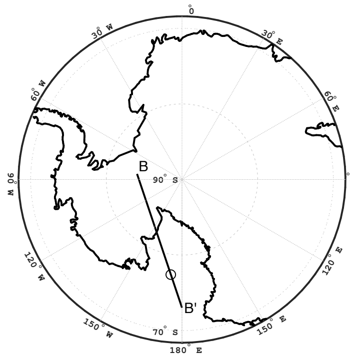

Figure 5.7: Location at the Ross Ice Shelf. The circle indicates the position where bedrock uplift is measured. The B-B' line indicates the line along where bedrock - ice shelf interaction will be showed.

In Figure 5.8 the uplift at the B-B" cut line is shown for the SLHE1D model from -20 kyr ago up to PD with 5 kyr time steps. At -20 kyr, the ice sheet is grounded at the o-marked location in the graph, that also corresponds with the location of the circle in Figure 5.7. At -15 kyr, the grounding line migrates to the left, which causes the bedrock to adjust to the reduction in ice loading. At -10 kyr and -5 kyr, the grounding line has migrated further left, causing large bedrock adjustment for the now unloaded bedrock. At PD, the bedrock is fully adjusted in the o-marked location.

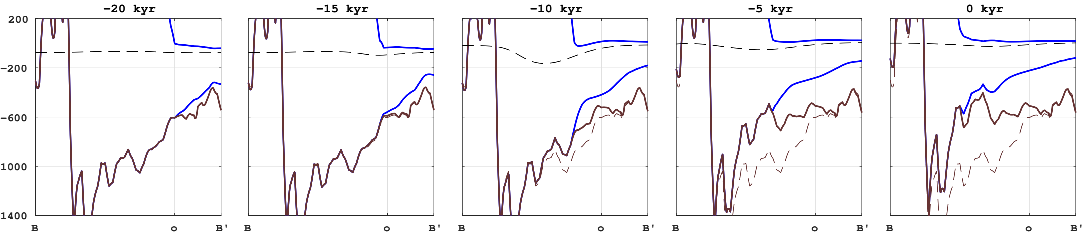

Figure 5.8: Bedrock uplift in the Ross region for the timeframe -20 kyr to PD with timesteps of 5 kyr. The used model is SLHE1D. Blue lines indicate the ice sheet/shelf, and the solid brown line indicates bedrock. The dashed brown line is the bedrock at -20 kyr, for reference purposes. The black dashed line is the geoid surface.

Figure 5.9 shows the bedrock adjustment properties for the o-marked location in Figure 5.7. Each model is represented by a separate curve and the properties are shown from -20 kyr to PD. The left figure shows the bedrock adjustment curves. The centre figure shows the ice volume and the right figure shows the relaxation times. The dot-dashed line corresponds with the SLHE1D model used in Figure 5.8.

In Figure 5.9a there is vast difference in the speed of bedrock adjustment. All adjustment curves start going upward at around -17 kyr. Thereafter, differentiation between the different curves is observed. This differentiation is also seen in Figure 5.9b, where the ice volume is shown for the Ross region. Here we see that at -10 kyr, two models have a slow down in melt-rate whereas other models show no significant reduction in melt. This behaviour will be discussed in subsection 6.1.1. Figure 5.9c shows the relaxation time of the different models. All models show a decrease in relaxation time around -10 kyr, due to a substantial reduction in ice sheet wavelength as shown in section 5.1. The relaxation times of the models are in agreement with the bedrock adjustment curves for the models. The SLHE1D and SLHE10W show quick bedrock movement, which is reflected by the small relaxation time value. The SLHE4D model shows large relaxation time values, and thus slow bedrock adjustment. The SL4D model's bedrock adjustment is close to the benchmark model, and so is its relaxation time.

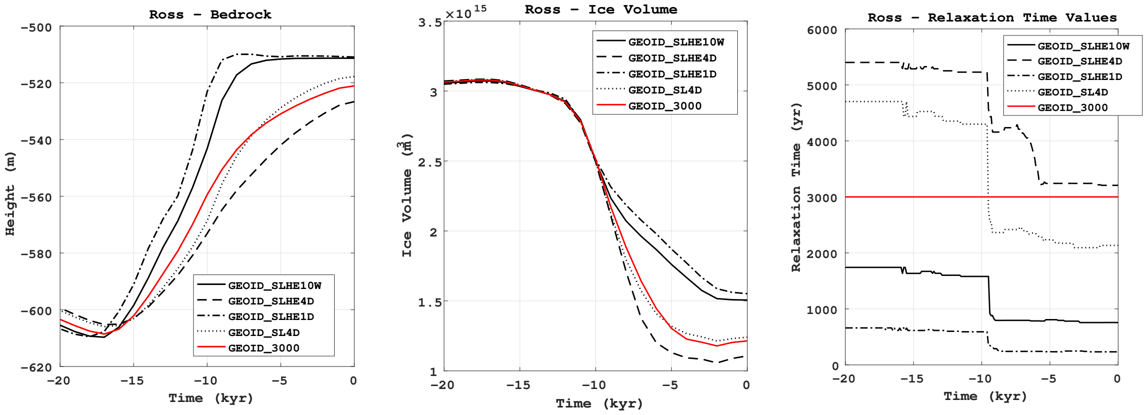

(a) (b) (c)

Figure 5.9: Properties of the Ross region. (a) indicates bedrock uplift for the indicated location. (b) shows the ice volume for the region. (c) shows the relaxation time. The timeframe for all figures is -20 kyr to PD.

Bedrock Uplift in the Ronne Region

For the Ronne region, the same properties are observed. The location marked with the circle in Figure 5.10 is grounded ice at LGM, but during the melt epoch this location becomes unconstrained and thus shows free bedrock deformation. The line A'-A indicates the position that is shown in Figure 5.11.

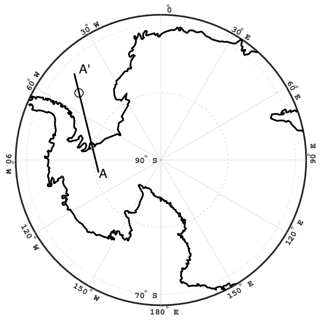

Figure 5.10: Location at the Ronne Ice Shelf. The circle indicates the position where bedrock uplift is measured. The A-A' line indicates the line along where bedrock - ice shelf interaction will be showed.

In Figure 5.11, the ice sheet is completely grounded on the continental shelf at -20 kyr. Once the melt epoch starts, a small retraction of the main dome can be seen at -15 kyr, together with a small ungrounding event. However, at -10 kyr a large change can be observed where the main dome shifts leftwards, along with the grounding line. At -5 kyr and 0 kyr this shift continues towards the elevated bedrock area.

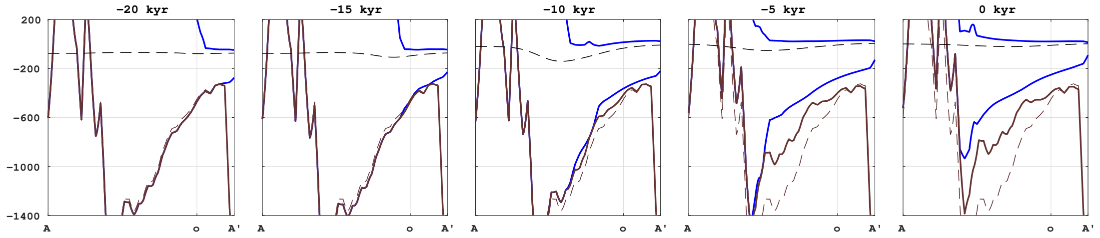

Figure 5.11: Bedrock uplift in the Ronne region for the timeframe -20 kyr to PD with timesteps of 5 kyr. The used model is SLHE1D. Blue lines indicate the ice sheet/shelf, and the solid brown line indicates bedrock. The dashed brown line is the bedrock at -20 kyr, for reference purposes. The black dashed line is the geoid surface.

In Figure 5.12, a collection of figures is shown in the same way as in Figure 5.9. The bedrock at the Ronne ice sheet at -20 kyr has not been fully adjusted to the ice loading, as there is still a downward trend in bedrock height. This is also observed in Figure 5.11, where the bedrock curve (solid) is below the reference bedrock curve (dashed) at -15 kyr, indicating ongoing adjustment to previous loading. Due to the large relaxation time of the SLHE10W model, the bedrock height for this model lags w.r.t. the other models. The SLHE1D model as well as the benchmark model have relatively small relaxation time and thus fast bedrock adjustment speeds. This reflects in the bedrock adjustment graph, where both models have rapid adjustment. The ice volume for these models is relatively large at PD. The SLHE4D and SL4D models have relaxation time values in the range of 5500 years and show comparable bedrock adjustment curves and ice volume curves.

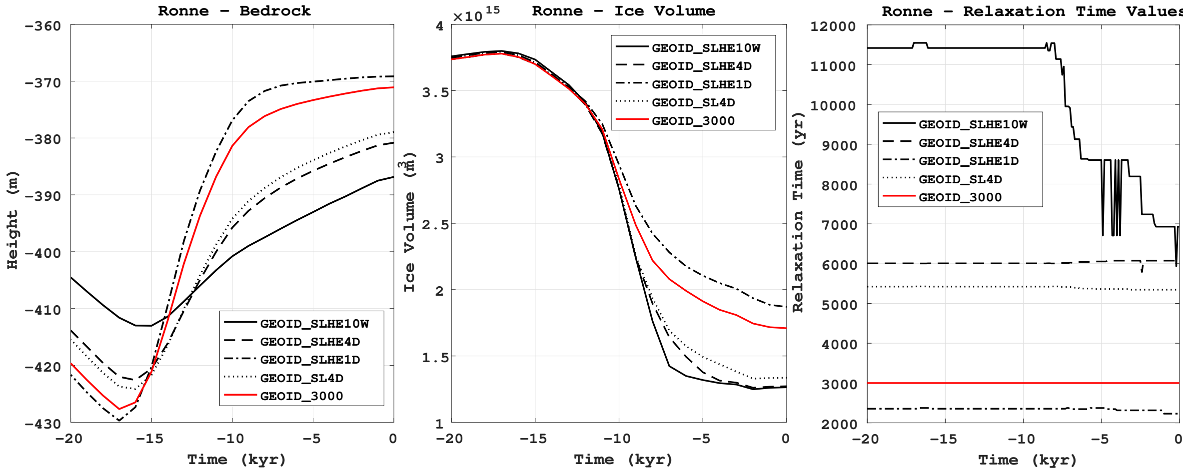

(a) (b) (c)

Figure 5.12: Properties of the Ronne region. The left figures indicates bedrock uplift for the indicated location. The centre figure shows the ice volume for the region. The right figure shows the relaxation time. The timeframe for all figures is from -20 kyr to PD.

5.3. Sensitivity Test on Ice Volume

To assess the significance of the results, a sensitivity test was performed for the SLHE1D model (largest ice volume at PD) and the SLHE4D model (smallest ice volume at PD). The last 20 kyr are shown in Figure 5.13. The grey curves surrounding the main curves are the envelopes in which the disturbed runs are contained. For each model, 3 configuration variables were altered, which lead to a combination of 8 (2^3) runs. The main run is the black line in Figure 5.13, and the other 7 runs are contained in the grey area.

In Table 5.2 the different sensitivity runs and their properties are shown. Sensitivity run # 0 indicates the main run that is considered the standard run. The three configuration variables are *m_enh_sia*, *m_enh_ssa*, and *subshelf_melt_factor*. Both *m_enh_sia* and *m_enh_ssa* enhance the flow in respectively the SIA domain and the SSA domain. The standard value for respectively *m_enh_sia* and *m_enh_ssa* is 5 and 0.7. An increased value for those parameters will increase the flow speeds in these domains. The *subshelf_melt_factor* parameter influences the amount of basal melt for ice shelves. Its standard value for AIS simulations is 0.005. Here, a smaller value for this parameter reduces the heat flux between ocean and shelf, and leads to an decrease in basal melt.

Table 5.2: Properties of each sensitivity run.

run #	m_enh_sia	m_enh_ssa	subshelf_melt_factor
0	5	0.7	0.005
1	7	0.7	0.005
2	5	0.8	0.005
3	7	0.8	0.005
4	5	0.7	0.003
5	7	0.7	0.003
6	5	0.8	0.003
7	7	0.8	0.003

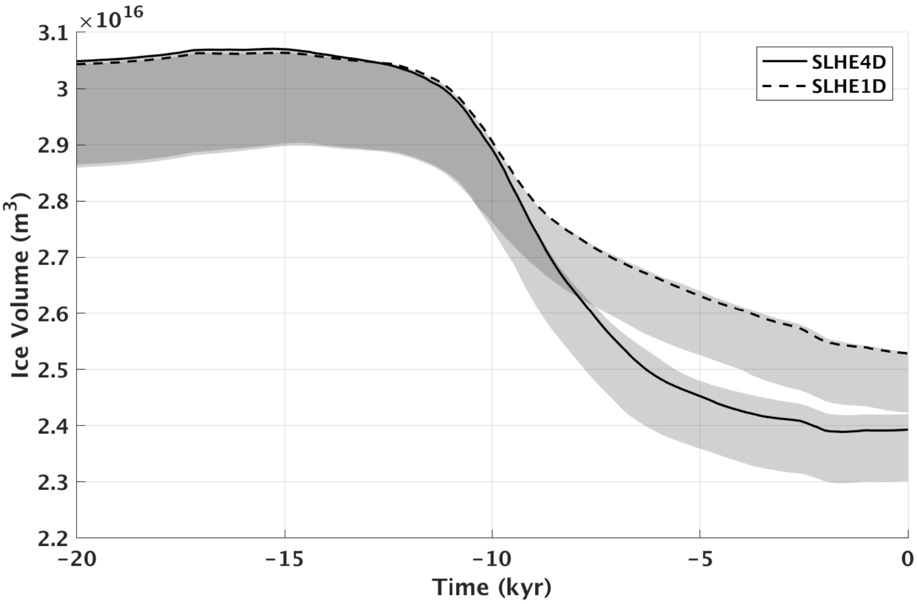

Figure 5.13: Sensitivity test results for the SLHE1D (dashed) and SLHE4D (solid) model. The gray patch surrounding the main curve is the envelope of disturbed runs.

In Figure 5.13 it can be seen that for both models, the undisturbed curve lies close to the ceiling of the disturbed envelope. It can be seen that there is no significant difference up to -15 kyr and both envelopes overlap completely. However, around -15 kyr differences occur and the curves diverge. At PD, there is no overlap in the disturbed runs for the SLHE1D and SLHE4D models, although the minimum value of the SLHE1D envelope is very close to the maximum value of the SLHE4D envelope. It shows that there is a significant difference between both models. Moreover, the width of the envelope for both models is about 4% of the total ice volume at PD.

6

Discussion

In this chapter, a more in depth discussion is presented considering the uplift of some models. The uplift data for the models is analysed, compared, and validated with ice volume data and basal melt data in section 6.1. Possible causes for uplift behaviour are presented. In section 6.2 an alternative explanation is presented for uplift in central ice sheet locations. Next to that, the wavelength determination module will be discussed in section 6.3.

6.1. Ungrounding of Ice Sheets In the Ronne and Ross Region

As shown in chapter 5, most ice melt occurs at the Ross and Ronne region, which makes these regions most interesting to observe. It was shown that for both regions, in the epoch from -20 kyr to PD, the grounded ice resting on bedrock below sea level almost completely became floating ice. In ANICE, ice shelves are subject to basal melt, which induces additional melt along the base of an ice shelf (De Boer, 2014).

6.1.1. Grounding Line Migration in the Ross Region: Different Viscosity Models Compared

In Figure 6.1 an overview of bedrock adjustment is shown for the SLHE1D model and the SLHE4D along the line shown in Figure 5.7. These two models are chosen because of the great differences in adjustment speeds between those two models. In the top frames the SLHE1D model is shown, and in the bottom frames the SLHE4D model. The most left figures show the ice sheet and bedrock at -20 kyr and the most right frames show the bedrock and ice sheet at PD. Each intermediate figure is shown with a timestep of 5 kyr.

For the Ross region, the SLHE1D has a relaxation time value of **700 yr** for the period from -20 kyr to -10 kyr, and **300 yr** from -10 kyr to PD. The SLHE4D model has a relaxation time of **5400 yr** for -20 kyr to -10 kyr, **4100 yr** for -10 to -7 kyr, and **3200 yr** from -7 kyr to PD. Hence, the SLHE1D model overall has quicker adjustment times relative to the SLHE4D model. This can be observed in the figure as well.

For -20 kyr and -15 kyr, both models behave in a similar fashion. However, at -10 kyr small differences occur: the SLHE1D model responds quick to the ungrounding of the ice sheet, causing little grounding line migration. The SLHE4D model responds slower, although the grounding line position is at the same location as for the SLHE1D model. Larger differences become apparent at -5 kyr. The SLHE1D has a larger bedrock adjustment due to the removed ice loading. The SLHE4D model has slower adjustment speeds, causing the bedrock to stay below the -600 meter line, whereas the SLHE1D model has reached up to about -500 meter for some points. The major effect of the rapid adjustment is that the ice sheet has found ability to ground itself on the bedrock relatively close to the LGM grounding line. For the SLHE4D model, a rapid detachment is observed and the ice shelf is only attached to the elevated bedrock at the left side of the frame. At PD, a small leftward shift can be observed for the grounding line in the SLHE1D model, but it stays grounded to the rising bedrock below sea level.

Furthermore, it was shown in Figure 5.2 that around -10 kyr, the relaxation time for all models decreased significantly due to the adaptive relaxation time method. For example, the SLHE1D model shows a relaxation time decrease from 600 yr to about 250 yr, which increases the uplift speed in the Ross region. Thus, the decrease in bedrock causes here a shift in relaxation time to smaller values for all models. The faster relaxation times make the bedrock lift up even quicker, giving the ice shelf a large opportunity to ground on the uplifting bedrock.

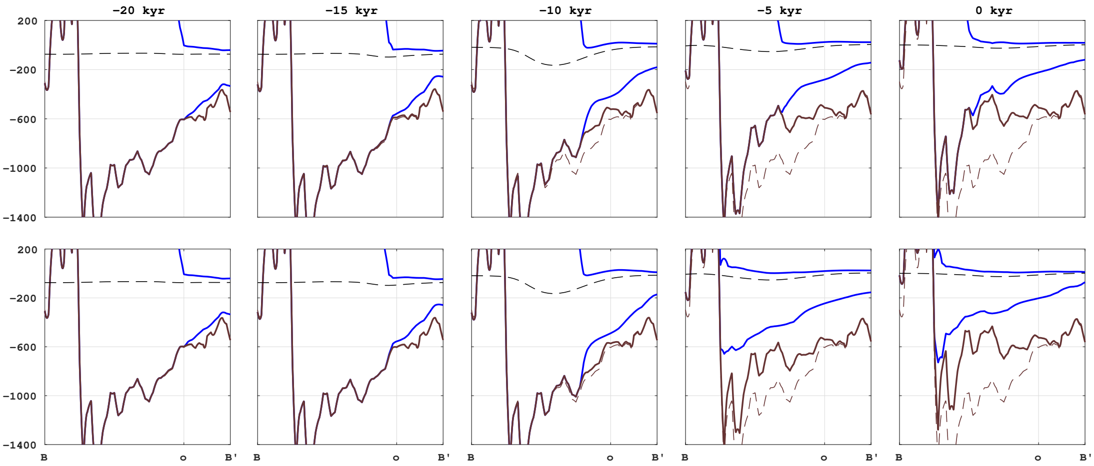

Figure 6.1: Bedrock uplift in the Ross region for the timeframe -20 kyr to PD with timesteps of 5 kyr. The used model is SLHE1D in the top figure, SLHE4D in the bottom figure.

An ice shelf are subject to mass fluctuation due to contact with ocean water along its base (De Boer et al., 2015). This could result in 1) ocean water refreezing, which would positively influence the mass balance and 2) basal melt, which would negatively influence the mass balance. In Figure 6.2 the basal mass balance ice shown for the Ross region. A blue mass balance indicates a positive value (refreezing), whereas red indicates a negative value (basal melt). Black indicates zero, which holds for grounded ice. The top row figures show the SLHE1D model, and the SLHE4D model is shown in the bottom row. At -12 kyr, both models do not show significant mass loss. At -8 kyr, both models show mass loss as well as mass gain. For the SLHE4D the mass loss region seems larger, which is due to the fact that the SLHE4D ice shelf is larger, and hence, more subject to melt. This is also seen in the frames from -4 kyr and PD, where the ice shelf for the SLHE4D model is larger. Overall, it is observed that the SLHE4D model has a larger ice shelf, which is more subject to mass loss through basal melt.

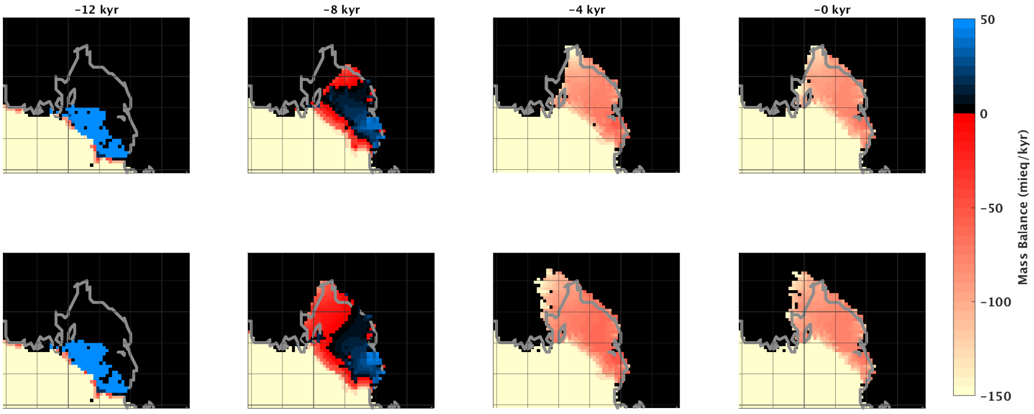

Figure 6.2: Basal mass balance for the Ross region for the SLHE1D model (top), and the SLHE4D model (bottom). Black indicates a mass balance of zero meter ice equivalent per kyr. Blue indicates a positive basal mass balance (refreezing) and red a negative basal mass balance (basal melt)

6.1.2. Grounding Line Migration in the Ronne Region: Different Viscosity Models Compared

A same approach is taken to examine the ice volume loss for the Ronne ice sheet. The SLHE1D and SLHE10W models will be compared here, as they show most differences bedrock uplift. The SLHE1D model has quickest uplift with a relatively constant relaxation time during the last 20 kyr of **2300 yr**. The SLHE10W uplift is slow with values ranging from **11500 yr** at LGM to **5000 yr** at PD. In Figure 6.3 the bedrock adjustment for both models is shown over the -20 kyr to PD period. The top frames show the SLHE1D model, and the bottom frames the SLHE10W model. At the -20 kyr and -15 kyr, only minor differences are observed between the models. At -10 kyr, the ice dome has shifted leftwards significantly, which results in a small bedrock adjustment for the SLHE1D model. This adjustment is not observed in the -10 kyr frame for the SLHE10W model, as its relaxation time is 11 500 years. The slow relaxation time results in a rapid grounding line retreat at -5 kyr. Although the relaxation time is reduced to values in the 6000 yr - 8000 yr range due to the adaptive relaxation time, it is not able to sustain a grounded ice sheet. The SLHE1D model, with a relaxation time of 2300 year, has rapid adjustment and the grounding line is closer to the original grounding line. At PD, the SLHE1D model is not able to maintain the grounded ice sheet but it still shows significantly more ice at this stage compared to the SLHE10W model.

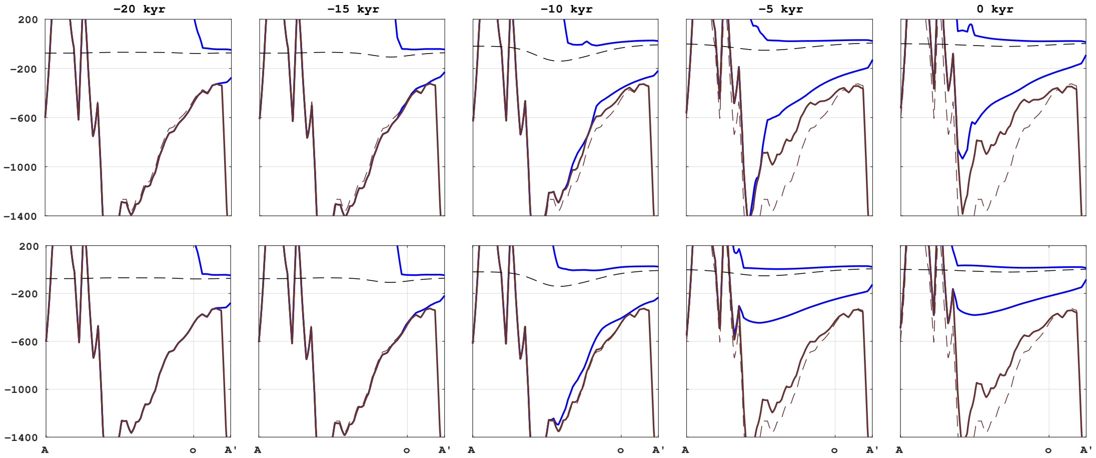

Figure 6.3: Bedrock uplift in the Ronne region for the timeframe -20 kyr to PD with timesteps of 5 kyr. The used model is SLHE1D in the top figure, SLHE10W in the bottom figure.

Figure 6.4 shows the basal mass balance for the Ronne ice shelf. The upper frames show the SLHE1D model, and the bottom ones the SLHE4D model. At -12 kyr, there is neglectable difference between the models and the shelf's mass balance is mainly positive (refreezing). At -8 kyr, the basal melt for the SLHE4D model has advanced further inland compared to the SLHE1D model. Here, the SLHE1D model is still grounded at the black surface points. This pattern continues for -4 kyr and PD, where the SLHE4D model has significantly more shelf area. Hence, the area subject to basal melt is larger for this model as well.

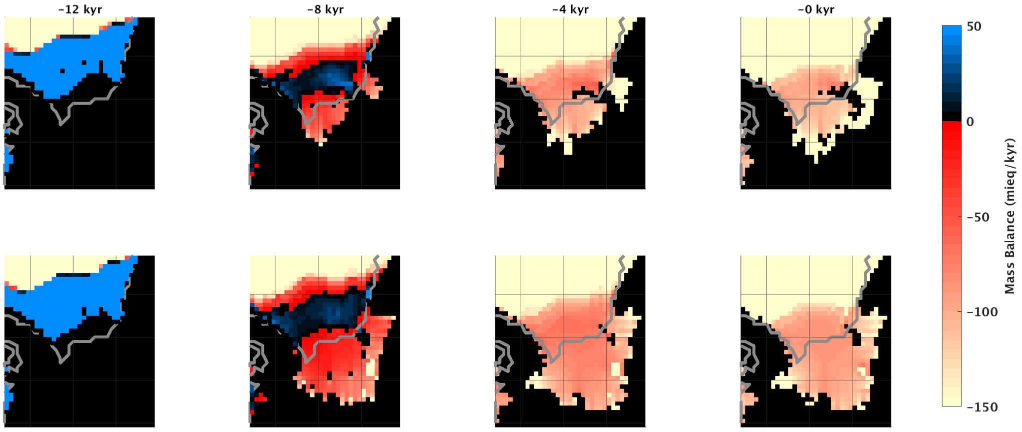

Figure 6.4: Basal mass balance for the Ross region for the SLHE1D model (top), and the SLHE4D model (bottom).

6.2. Bedrock Uplift Rate Constrained by Slow Melt Rate

In the previous sections, bedrock uplift was mainly unconstrained. That is, the bedrock uplift was not loaded by any form of ice. This is the case for regions where ice shelves form, which is mostly at the ice sheet margins. However, bedrock that is situated in the area where the Antarctic Ice Sheet is permanently grounded can not always adjust unconstrained. The uplift here is constrained by the remaining ice loading on the bedrock.

Figure 6.5 shows several properties at an upstream location in the Amundsen region, with grounded ice. Figure 6.5a shows the local ice height for different models, Figure 6.5b shows the bedrock uplift for different models, and Figure 6.5c shows the relaxation time for the different models. The ice height decreases around -12 kyr, and different models start to diverge. Although there is a clear difference in ice height between the models, the relative ice height decrease is small (8.4% for the SLHE1D model, 11.5% for the SLHE4D model). Despite the differences in ice height, no major difference in bedrock uplift for the different models in the -10 kyr to -5 kyr timeframe is seen. In Figure 6.5c the relaxation time for the different models is shown. Differences in relaxation time go up to 2400 years and from these values a difference in uplift would be expected.

From -5 kyr to PD there is ice height and bedrock uplift difference between the models, where it is seen that the bedrock adjustment rates are in accordance with their respective relaxation time values, as was seen for the Ronne and Ross regions. The cause for the larger change only occurring in the last 5 kyr could be attributed to the remoteness of the location. Figure 6.5 is taken at a position upstream, distant from ice sheet margins. Largest changes in ice height occur along the ice sheet margins, and it takes time for large changes to propagate towards the central parts of the ice sheet due to the finite internal velocities of the ice sheet. Therefore, when melt at the margins occurs at e.g. -10 kyr, differences upstream might be observed only in the last e.g. 5 kyr.

This however does not explain the equal bedrock uplift from -10 kyr to -5 kyr for all models. There are clear differences in ice height decrease for this same time span, which would induce differences in bedrock uplift. A proposed explanation is that the melt rate, and hence the ice height decrease is to slow to induce bedrock uplift differences between the models. Here, bedrock uplift is not constrained by relaxation time, but by melt. Here, we see that the differences in ice loading between the models are not large enough to induce significant differences between models in the bedrock uplift.

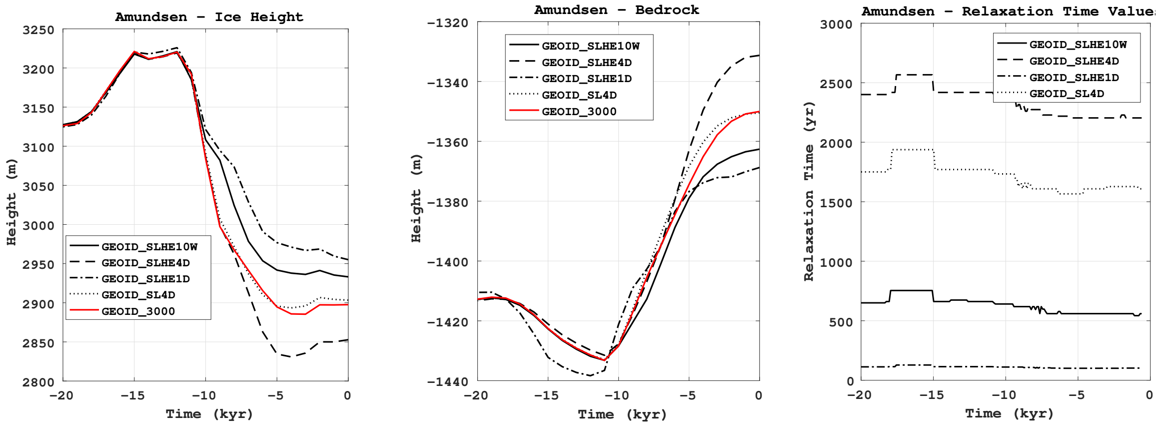

(a) (b) (c)

Figure 6.5: Uplift in the Amundsen area. (a) shows the ice height in meters at the upstream location. (b) shows the bedrock uplift. (c) shows the relaxation time values for the different models.

6.3. Isolated Regions and Wavelength Determination

The method used for adaptive relaxation time determination finds the longest distance between two points that remain after filtering for ungrounded, negative and outer region points. The routine filters for isolated ice points in the grid, to prevent small island being considered in the distance determination. This filter however does not always function appropriately.

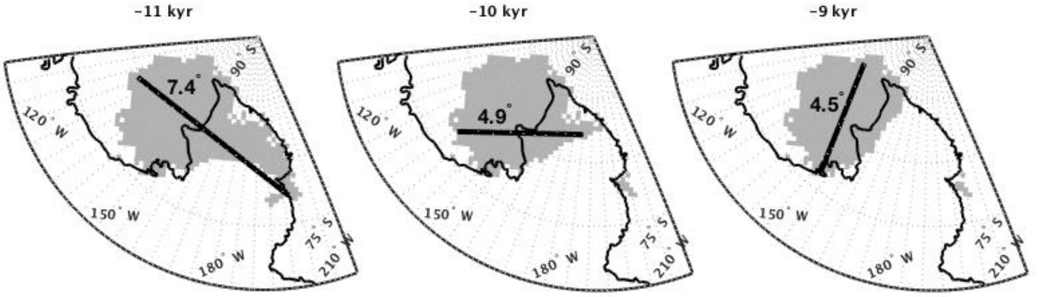

Figure 6.6: Wavelength development for the Ross region at -11 kyr, -10 kyr and -9 kyr.

Figure 6.6 shows the determined wavelength at -11, -10 and -9 kyr. The determined wavelength seems to be correct. Furthermore, on the right side of the frames, an isolated grey area can be seen (75S, 200W), which is not taken into account. This is correct behaviour, because the isolated area does not contribute to the wavelength of the main ice dome.

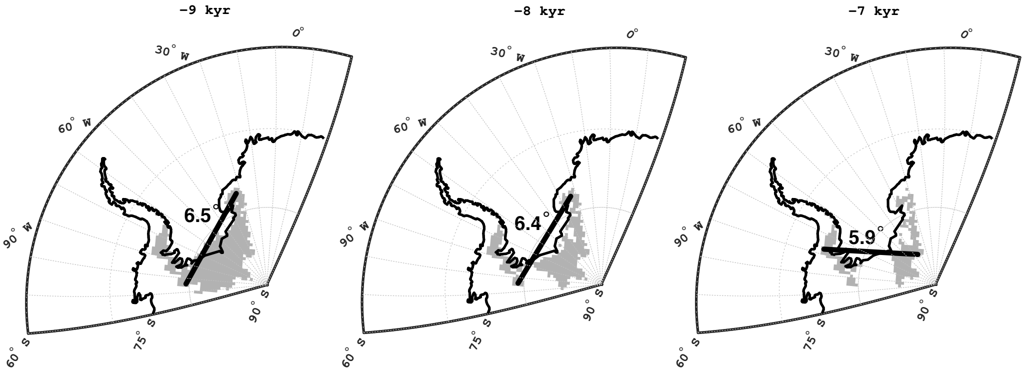

Figure 6.7: Wavelength development for the Ronne region for -9 kyr, -8 kyr and =7 kyr.

In Figure 6.7 the same frames are shown for the Ronne ice sheet. Here we see unwanted behaviour of the routine. At -9 kyr the wavelength seems correct, but at -8 kyr a separation forms between an eastern and western part of ice sheet. Both parts are relatively large, and are both not discarded in the wavelength determination process. That is why the wavelength is being overestimated. In this case, only the largest region should be taken into account and the wavelength should only be computed for this region. This will result in a smaller wavelength for the complete region. Next to that, the observed ice cap has a crescent shape. Once the shape of the ice cap becomes less circular, the determined wavelength becomes less accurate as well.

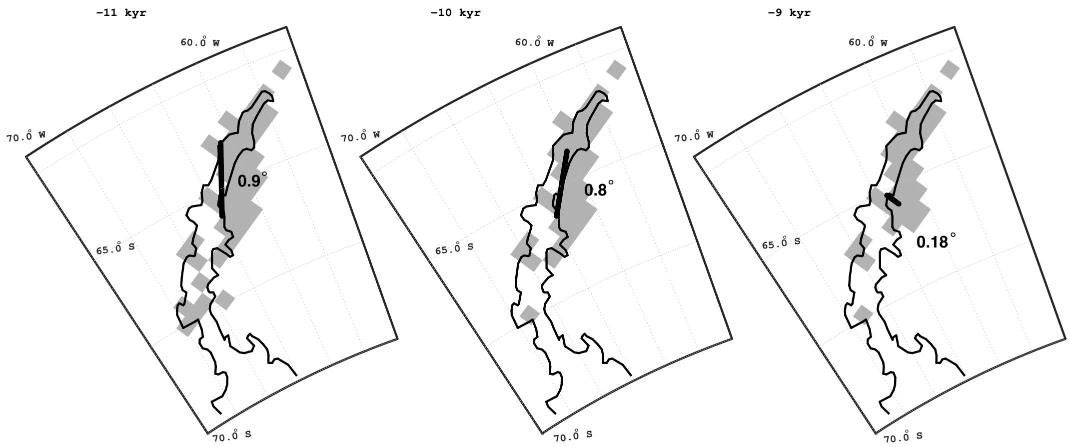

Figure 6.8: Wavelength development for the NAP region for -11 kyr, -10 kyr and -8 kyr.

Figure 6.8 Shows the NAP region with the determined wavelengths. At -11 kyr the estimated wavelength is 0.9°. Here, we see that the method discards many points that are not part of the main region but are only loosely connected. At -10 kyr the main dome shrinks a small amount to 0.8°. At -9 kyr, the wavelength shrinks to 0.18° which is the minimum distance (distance between two gridpoints). This implies that the routine was not able to find two points that met all filtering criteria. Hence, here all points are labeled as isolated.

For large, consistent ice domes, such as the Ross region, the module behaves as expected. However, it shows unwanted behaviour for the following cases:

- The ice cap shrinks to a relatively small size where no points remain unfiltered.

This is the case for the NAP region, where no points remain after filtering. The effect of this is small, because this effect happens only for very small wavelengths. The smallest wavelength for which a relaxation time is known is 0.625°. For any wavelength of an ice cap below this value, the relaxation time is automatically set to the relaxation time associated to the 0.625° wavelength. As shown in Figure 6.8, the wavelength where the ice cap becomes too small, is under 0.8°. As this value is already close to 0.625°, the difference in computed and correct relaxation time is expected to be small.

- The ice cap splits into several isolated ice caps.

This is the case for the Ronne ice cap. The ice splits in two smaller ice caps, but the wavelength is still computed as if it is one large ice cap. The computed size is around 6°, whereas both smaller ice caps are about 4°. The relaxation time error induced by this wrong computation is ±200 year for all models except the SLHE10W model, where it is ±1000 year. For the Ross region, it was seen that the relaxation time reduced when the wavelength of the sheet reduced. From wavelength-relaxation time values, it can be observed that this would be the case for the Ronne region as well. If the module would predict relaxation time values more accurately it would predict smaller wavelengths and smaller relaxation times would be the result. For all models, this would lead to an increase in rebound and possibly less melt due to less grounding line migration.

- The ice cap has an non-circular shape.

The normal mode model that is used to determine the relaxation times was forced using a circular ice cap. However, ice caps do not follow a perfect circular shape. For example, the Ronne ice cap is crescent-shaped and the determined wavelength is not necessarily the wavelength that would match the wavelength for a perfectly circular ice cap. A difference in wavelength prediction could be expected if a more suitable method would be used for this. However, expected are only small relaxation time differences in the order of 100-500 years.

7

Conclusions

In this thesis, the ANICE ice model was used to simulate the Antarctic Ice Sheet (AIS) development in the period from -120 000 years ago to PD. The model uses eustatic sea level and temperature as main forcing to simulate grow and melt. ANICE uses Glacial Isostatic Adjustment (GIA) to include bedrock relaxation in the model. In existing literature ice *dynamic* simulations of the AIS are performed with laterally *constant* bedrock properties or simulations are done with *laterally* varying bedrock properties, but only with a *static* ice model. In this thesis, the focus lies primarily on the use of laterally varying bedrock properties in the ice dynamic model and the effects of this.

For an accurate simulation of the AIS, sea level forcing is crucial. A large part of the melt occurs through contact with ocean water along the ice sheet margins and ice shelves (Weertman, 1974). The sea level along the ice sheet margins is therefore an important parameter. Eustatic sea level varies with respect to local sea level due to gravitational effects. The ANICE model was run in combination with SELEN, resulting in a gravitationally self-consistent sea-level map for Antarctica (De Boer, 2014). This geoid sea level forcing was used in a standard ANICE model and compared against the standard model with eustatic sea level forcing. During the build-up phase (-120 kyr to -20 kyr), the eustatic forcing resulted in a larger ice sheet volume, whereas the PD ice sheet volume for the eustatic model was smaller compared to the geoid forcing. This was expected, as geoid forcing has a negative feedback on ice sheet development, mainly through the self-gravitation of the ice sheet (De Boer, 2014). Since the geoid defines the sea surface in a more accurate way, the geoid forcing was used in future models.

To answer one of the main research questions (how can a laterally varying relaxation time be used in an ice dynamic model?) it was found that, in order to use laterally varying relaxation time in ANICE, viscosity maps must be converted to relaxation time. van der Wal et al. (2015) used seismic wave models in combination with grain size and water content parameters to compute viscosity maps based on different ice loadings. This resulted in a broad set of viscosity maps dependent on grain size, water content, and seismic model choice. Five key Antarctic regions were identified to be of importance based on ice sheet behaviour and earth rheology parameters.

To include the relation between ice sheet wavelength and the deformation mode of the mantle, a normal mode model was used to predict uplift curves. For a series of ice caps with varying wavelength Whitehouse et al. (2017b) generated displacement curves for each region based on the layered viscosity maps. The dominant uplift mode in each displacement curve was converted to a relaxation time. This was done by filtering the displacement curves and through curve fitting, a series of relaxation times were estimated for each region. Four different models, the SLHE1D, SLHE4D, SLHE10W, and SL4D were selected for usage with the ANICE model, based on uplift data fits and found grain size samples (van der Wal et al., 2015). The excited uplift mode of the mantle is wavelength dependent, and this dependency is inherited to the determined relaxation times. The ANICE model was adjusted to be able to determine the wavelength of the ice caps in each of the five regions during runtime.
The adaptive relaxation time method is based on a largest distance finding routine. It finds the maximum distance along the ice sheet border points. The method discards points that lie outside the main ice sheet or points that are isolated. It was found that for large, circular-shaped ice sheets, this routine works as expected. However, for several cases difficulties exists. One major drawback is the inability to find large ice sheet separations. This occurred in the Ronne region only and it lead to errors in relaxation time of ±200 years for all models, except the SLHE10W model, where it lies around ±1000 years.

The SLHE1D, SLHE4D, SLHE10W, and SL4D relaxation time models were used as input fields for the relaxation time, in the ANICE runs with the geoid forcing and adaptive relaxation time. The reference model is considered to be the geoid forcing model with a constant relaxation time of 3000 years. It was found that all four models showed slightly larger volumes during the build up phase (-120 kyr to -20 kyr). The melt epoch from -20 kyr to PD however shows large differentiation between the models, where the largest melt was observed for the for the SLHE4D (largest average relaxation time) model and the SLHE1D model (smallest average relaxation time) showed the smallest volume loss.

As most melt occurs in the Ross and Ronne region, these regions were examined more specifically. In the Ross region, the SLHE1D model, having lowest relaxation time values, showed the least volume loss. The SLHE4D model, with highest relaxation times in the Ross region, showed the largest volume loss here. For the Ronne region, where the SLHE1D model has the smallest relaxation times as well, the SLHE1D model showed the smallest volume loss. It was the SLHE10W model that showed the largest mass loss in the Ronne region, closely followed by the SLHE4D model. Those two models had the largest relaxation time values for the Ronne region.

The main reason for the large mass loss in the Ross and Ronne region is due to rapid grounding line migration. When an ice shelf forms, it is subject to basal melt. Due to contact with ocean water, basal ice melts and hence, mass loss occurs. It was found that for models with quick uplift rate, the grounding line migration in both the Ronne and Ross region is less rapid compared to the models with slow uplift rates. This is in agreement with previous literature (Schoof, 2007; Weertman, 1974), that predicts less grounding line migration for quick uplift near ice sheet margins.

The constant relaxation time of 3000 years that is widely used in literature (Le Meur and Huybrechts, 1996; van den Berg et al., 2008a; Whitehouse et al., 2012) might give acceptable ice volumes for the complete AIS. It does however not capture the strong relation between grounding line migration and relaxation time in the WAIS. It was shown that relaxation time values can reach values of 100 yr in the WAIS for some models, and that significant differences occur compared to relaxation times of 3000 yr. For ice sheet parts that reside on the central part of the continental shelf, relaxation time is of less significance. It was shown that for those regions, bedrock adjustment is sometimes constrained by the rate of melt. At these locations, changes in ice height are not large enough to distinguish between different uplift rates.

The rapid reduction of grounded ice around -10 kyr induced a wavelength decrease in nearly all regions. Due to the adaptive relaxation time module, this lead to a reduction in relaxation times for nearly all models. Relaxation times were reduced with 40% to 60% in the Ross region. This reduction in relaxation time results in even faster uplift, which prevents further grounding line migration. This stabilising mechanism could prevent the complete ungrounding of an ice shelf and reduce mass loss. Fast bedrock adjustment shallows sea level, which reduces ice flux towards the oceans. This prevents severe mass loss for regions further upstream (Feldmann and Levermann, 2015; Gomez et al., 2015, 2013; Huybrechts, 1990). This mechanism only has a stabilising effect when relaxation time decreases with decreasing wavelength. Most models prescribe such a relation, but for some models, non-linear behaviour is observed. There is no indication to what extent this mechanism provided stabilisation in the shown simulations. In the Ross region, this mechanism clearly showed its functionality by reducing relaxation times with 40% to 60%. However, there is no to very little wavelength adaption in the Ronne region. It was found that this was mainly due to inconsistencies in the wavelength determination process, which resulted in wavelengths close to LGM wavelengths.

Bedmap2 predicts a total ice sheet volume of 26.92 million km^3 for the Antarctic Ice Sheet at PD (Fretwell et al., 2013). All simulations are below this value, with the SLHE1D model being closest with an ice volume of 25.28 million km^3. The small grain size and high water content of the SLHE1D model lead to low viscosity values in all regions. The low viscosity values reduces relaxation times significantly for each region. The effect of the reduced relaxation time was obvious in the Ross and Ronne region. The SLHE10W model showed high viscosity values for the Ronne region, and small viscosity values for other regions. In turn, this resulted in large melt quantities in the Ronne region but to a lesser extent in the other regions. The SLHE4D and SL4D model showed the largest viscosity values and corresponding relaxation times when considering all regions. This was also reflected in the total ice volume: The largest decrease in ice volume was seen in the SLHE4D model, closely followed by the SL4D and SLHE10W model. The SLHE1D model showed 3.5 m SLEQ more ice volume compared to the SLHE4D model. A sensitivity analysis showed a significant differences between both models.

8

Recommendations

It remains unclear to what extend the adaptive relaxation time method affects ice volume development. It was shown that there was a change in relaxation time with changing ice sheet wavelength, but it remains unknown how greatly it affects grow and melt. Running the ANICE model both with and without this adaptive method for each relaxation time model would provide insight in ice volume differences and the significance of the adaptive relaxation time method.

Furthermore, many different models are coupled together to compute values required by the ANICE model. The conversion from viscosity models to relaxation time models involves errors of which the sizes are not precisely known. Specifically, approximations are made in the conversion from the complex rebound signal produced by the normal model, to a single relaxation time. Here, part of the rebound signal is lost which would normally affect the uplift on longer timespans.

One solution to this problem is using a coupled 3D-finite element earth with an ice dynamic model. Although this implementation is more accurate and elegant, it is also more time consuming. The method used in this thesis provides useful insight to the response of a laterally varying bedrock to melt and grow of an ice sheet. The question is if a more accurate model leads to better results. As the viscosity and seismic models have relatively large error margins, using a more accurate model will maybe not necessarily lead to more accurate results. The focus should lie on a more sophisticated way of converting viscosity to relaxation time.

8.1. Specific Recommendations for the Adaptive Relaxation Time Routine

It was shown that the adaptive relaxation time module works for the cases where the ice cap has a regular circular shape and has a size larger than 1° wavelength. It was found that for three cases the module does not perform optimal. For two of those cases, the relaxation time is chosen incorrectly.

The routine must be updated to perform well in the cases where the ice cap has an irregular shape. Here, one could for example compute the surface area of the irregular shape, and set the wavelength to the radius of a circle with that same area. This would still be an assumption of the real wavelength of the ice cap, but it might reduce errors in some way. The underlying question is how earth's mantle responds to irregular shaped loadings, which would require simulations with irregular shaped ice caps in e.g. a normal mode model or a FEM model.

The other case where the module produces irregular results is when the remaining melting ice cap splits into two different caps. Here the module tracks all points as if it is one ice cap, and thus the determined wavelength is too large. In such case, the right solution would be to track both ice caps separately, and determine wavelengths and relaxation times for both ice caps separately. This approach is more sophisticated compared to the approach taken in this thesis and could deliver more accurate results. However, it would require some extensive programming as it requires some sort of island detection.

A

Ice Sheet Dynamics

Ice sheet behaviour is modelled using mass balances for exterior mass change. Interial mass transport is modelled through the shallow ice approximation for the main sheet and shallow shelf approximations for the shelf. Nowadays, the most widely used models use the shallow-ice approximation or SIA (De Boer et al., 2013; Schoof and Hewitt, 2013; van den Berg et al., 2008b; van der Veen, 1999).

A.1. Mass Continuity of the Ice Sheet

The mass continuity equation is the main starting point in ice sheet modelling. It applies a shallow ice approximation that uses the low aspect ratio of the ice sheet to simplify the Navier-Stokes equation (Schoof and Hewitt, 2013). The vertically integrated continuity equation in Equation A.1 is one of the shallow water equations, which in turn are derived from the Navier-Stokes equations (van der Veen, 1999). The shallow water equations are the governing equations for water motion in oceans, lakes, rivers, etc. The main assumption is that the water body is that the vertical dimension is much smaller than the horizontal dimension. Equation A.1 is taken from Schoof and Hewitt (2013):

$$\frac{\partial H_i}{\partial t} = -\nabla \cdot (H_i \mathbf{u}) + B \tag{A.1}$$

Here, H is the height of the ice, t is time, **u** is the vertically integrated horizontal velocity profile, and B is the mass balance per unit time.

The equation states that the change in height of the ice sheet depends on the divergence of the vertically integrated velocity field at that point. A positive divergence, which means that more ice is flowing away than flowing in, will reduce the height. Therefore, the minus sign corrects the equation. This is caused by the movement of ice due to sliding and/or movement due to compression.

The two most important parameters in Equation A.1, **u** and B, will be discussed in section A.3 and section A.2, respectively.

A.2. Mass Balance

The mass balance is the difference between mass loss and mass gain. B can be written as

$$B = P - M \tag{A.2}$$

where P is the amount of precipitation and M is the amount of melt per unit time.

The amount of precipitation P is a function of amount of water vapour in the atmosphere W. van den Berg et al. (2008b) approximates W by

$$\frac{\partial W}{\partial t} = -\mathbf{v} \cdot \nabla W - (f_0 + f_1 S)\, W + (W_m - W)\,/t^* \tag{A.3}$$

in which the first term describes the advection of moist air, the second term describes the precipitation and the third term describes the evaporation. In the advection term, $\mathbf{v}$ is the horizontal wind field. In the precipitation term, f_0 is the background precipitation constant, f_1 is the constant governing precipitation caused by saturation of upslope forced air, where S is the slope term. In the evaporation term, W_m is the maximal amount of water vapour and t^* is the characteristic time scale (van den Berg et al., 2008b). From the moisture balance an indication for precipitation can be given using other models such as HADCM3M2 and PMIP2, where temperature models indicate if the moisture falls as dry or wet precipitation (van den Berg et al., 2008a).

The amount of melting M in Equation A.2 can be approximated by

$$M = \Delta t \cdot [\tau\,(1 - \alpha)\, Q + c + 10T]\,/\,(1000 L_m) \tag{A.4}$$

in which M is the monthly melt in meters water. Δt is the amount of seconds in a month, τ is the transmissivity of the atmosphere, α is the albedo, $c + 10T$ is the sum of longwave radiation and turbulent exchange, T is the surface temperature in degrees Celsius, Q is the monthly insolation at the top of the atmosphere and L_m is the latent heat of melt (van den Berg et al., 2008a,b).

A.3. Internal Velocities

The horizontal velocity can be written as a combination of the sliding velocity and the deformation velocity, as in Equation A.5 (van den Berg et al., 2006).

$$\mathbf{u} = \mathbf{u_s} + \mathbf{u_d} \tag{A.5}$$

Here, $\mathbf{u_s}$ and $\mathbf{u_d}$ are the sliding velocity and the deformation velocity, respectively. In van den Berg et al. (2006) it is stated that if the sliding velocity is smaller than the deformation velocity, the sliding velocity may be neglected. For the deformation velocity two regions are used for mathematical formulation. The SIA approach is uded for the central part of the ice sheet, where the horizontal shear stress is dominating. For the region closer to the boundaries of the ice sheet, or where the shelf begins, the shallow shelf approximation (SSA) is used (Bueler and Brown, 2009; De Boer et al., 2013).

A.3.1. Shallow Ice Approximation for Ice Flow

in the SIA region, the horizontal shear stress is assumed to be large with respect to the normal and longitudinal stresses (see Figure A.1). The shear stresses are a result of the vertical differences in horizontal velocity (De Boer et al., 2013). The SIA ice flow within the ice sheet is computed by equating the weight of the ice sheet to the horizontal shear stress (De Boer et al., 2013). This approximation results in the following equation for horizontal velocity (Bueler and Brown, 2009; van de Wal, 1999):

$$\mathbf{u}_{SIA} = -2\left(\rho_i g\right)^n |\nabla H_s|^{n-1}\nabla H_s \int_b^z A(T^*)(H_s - z)^n \mathrm{d}\xi, \tag{A.6}$$

In which ∇H_s is the slope of the horizontal surface, ξ is the scaled vertical coordinate, g is gravity, ρ_i is the density, $A(T^*)$ is the flow-rate factor, as shown in van de Wal (1999). n is the Glen's flow-law exponent. For ice sheet modelling, n is usually assumed 3 for ice (Pattyn, 2003; van den Berg et al., 2008a,b, 2006). A is dependent on several ice parameters like purity and size, as well as temperature.

Since the SIA approach offers no capability to incorporate sliding stresses, the approach assumes no basal sliding: $u_b = 0$. This assumption reduces the friction at the base of the ice sheet, leading to less melt at the base of the sheet. Some models that incorporate a basal sliding velocity use a sliding law that is a function of the driving stress. According to Bueler and Brown (2009), the driving stress is the hydrostatic pressure at the base multiplied by the surface slope: $u_b = f(\rho_i g H|\nabla h|)$. The downside of incorporating a sliding law with the SIA approach is unreasonable flow results for denser grids (Bueler and Brown, 2009). In the next subsection the SSA model is discussed, which does incorporate longitudinal stresses (sometimes called membrane stresses).

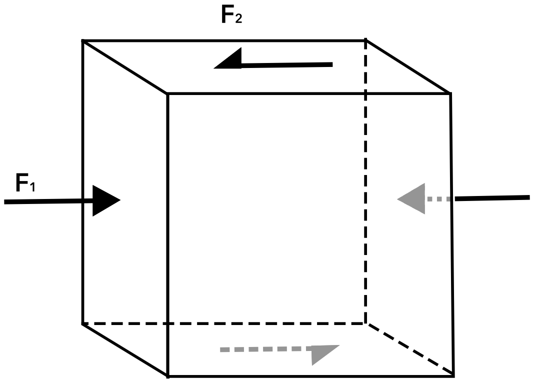

Figure A.1: Schematic overview of main stresses acting in the interior of an ice sheet. F_1 depicts the longitudinal normal stress which is neglected in the SIA approach. F_2 is the horizontal shear stress.

A.3.2. Shallow Shelf Approximation for Ice Flow

When moving closer to the boundary of the ice sheet, longitudinal stresses are becoming larger with respect to the horizontal shear stress (F_1 in Figure A.1). The SIA approximation therefore does not hold anymore. In the SSA model, the fluid is modelled as a fluid in which gravity causes spreading (Bueler and Brown, 2009). When this is applied to ice streams, shear forces do act at the base of the fluid (MacAyeal, 1989). The equations that govern the ice flow along the margins are given by (from (Bueler and Brown, 2009; MacAyeal, 1989; Pollard and DeConto, 2007)):

$$\frac{\partial}{\partial x}\left[2\mu_{va}H_i\left(2\frac{\partial u}{\partial x}+\frac{\partial v}{\partial y}\right)\right]+\frac{\partial}{\partial y}\left[2\mu_{va}H_i\left(2\frac{\partial u}{\partial y}+\frac{\partial v}{\partial x}\right)\right]+\tau_{b,x}=\rho_i g H_i\frac{\partial H_s}{\partial x} \tag{A.7}$$

$$\frac{\partial}{\partial y}\left[2\mu_{va}H_i\left(2\frac{\partial v}{\partial y}+\frac{\partial u}{\partial x}\right)\right]+\frac{\partial}{\partial x}\left[2\mu_{va}H_i\left(2\frac{\partial v}{\partial x}+\frac{\partial u}{\partial y}\right)\right]+\tau_{b,y}=\rho_i g H_i\frac{\partial H_s}{\partial y}, \tag{A.8}$$

in which u and v are the velocities in x and y direction in meters per year. μ is the vertically averaged viscosity and $\tau_{x,y}$ are the basal stresses. H_i is again the ice sheet thickness. H_s on the other hand is the surface elevation for ice shelves, which is equal to $(1-\rho_i/\rho_w)H_i$. In Equation A.7 and Equation A.8 the deformation stresses are balanced by the gravitational stress together with the basal stress. The basal stress is then computed by a Weertman type sliding law, which in turn is dependent on the basal sliding velocity (De Boer et al., 2013).

The velocities that are computed in the SIA and/or SSA approach function as input for the governing ice equation shown in Equation A.1. Together with the previously shown mass loss and gain, the ice height for each point in the ice sheet can be computed.

B

Geoid Routine for ANICE

In this appendix, the SELEN routine in the ANICE model will be further evaluated. The SELEN routine itself is not used for the models that are used for the results. However, the geoid file that is used in the models is created by using the SELEN routine. That is why here a discussion of the Sea Level Equation (SLE) and the SELEN routine will be given.

B.1. Geodynamics and the SELEN Routine

The following mathematical derivation comes from Spada and Stocchi (2007). In chapter 3 it was shown that the sea level variation S is the difference between the sea surface variation and the vertical displacement of the bedrock U:

$$S(\omega, t) = N(\omega, t) - U(\omega, t). \tag{B.1}$$

The sea surface variation N is closely related to the geoid height variation G:

$$N(\omega, t) = G(\omega, t) + c(t) \tag{B.2}$$

where c functions as mass balance conservation term. The geoid height variation, G, can be written as

$$G(\omega, t) = \frac{\Phi}{\gamma}. \tag{B.3}$$

In this equation, Φ is the variation of the gravity potential. γ is the reference gravity at the surface of the earth. Combining Equation B.2 and Equation B.3 gives

$$S(\omega, t) = \frac{\Phi}{\gamma} - U + c. \tag{B.4}$$

To ensure mass conservation between ice sheets and ocean water, the c term can be written as:

$$c(t) = -\frac{m_i}{\rho_w A_0} - \overline{\left(\frac{\Phi}{\gamma} - U\right)}. \tag{B.5}$$

Here, m_i is the mass variation of the ice sheet, ρ_w the density of water, A_0 the present day area of the oceans, and the overbar performs an average over the oceans surface. Taking Equation B.4 and Equation B.5, the resulting equation can be written as

$$S(\omega, t) = \left(\frac{\Phi}{\gamma} - U\right) + S^E - \overline{\left(\frac{\Phi}{\gamma} - U\right)}, \tag{B.6}$$

where the eustatic sea level varation is reduced to S^E:

$$S^E(t) = -\frac{m_i}{\rho_w A_0}. \tag{B.7}$$

The terms U and Φ are mostly dependent on the surface load on earth, that is, the mass distribution of water and ice. In mathematical form, the mass distribution ζ is written as:

$$\zeta(\omega, t) = \rho_i I + \rho_w S O. \tag{B.8}$$

In this equation, I is the ice thickness variation, ρ_i is the density for ice, and O is the ocean function. The ocean function is 1 for each point that is ocean, and zero for continental points:

$$O(\omega) = \begin{cases} 1, & \text{if ocean} \\ 0, & \text{if land.} \end{cases} \tag{B.9}$$

The ice thickness variation in Equation B.8 is the difference between the ice thickness at time t and a reference point in history. Ice thickness variation can therefore be written as

$$I(\omega, t) = T - T_0. \tag{B.10}$$

The previously mentioned mass variation m_i can be obtained by integrating the ice thickness variation I over the surface of the earth. The vertical displacement of the bedrock involves two terms, namely one that stems from ice load, and one that stems from ocean load:

$$U(\omega, t) = \rho_i G_u \otimes_i I + \rho_w G_u \otimes_o S \tag{B.11}$$

where G_u is the Green's function for vertical displacement. $\otimes_{i,o}$ is the spatiotemporal convolutions for the ocean and ice covered regions. For the gravity potential, a similar equation can be written:

$$\Phi(\omega, t) = \rho_i G_\Phi \otimes_i I + \rho_w G_\Phi \otimes_o S \tag{B.12}$$

The Green’s function for the sea level can be written as:

$$\frac{G_s}{\gamma}(\omega, t) = \frac{G_\Phi}{\gamma} - G_u \tag{B.13}$$

Substituting Equation B.11 and Equation B.12 into Equation B.6 and rewriting using Equation B.13 gives

$$S(\omega, t) = \frac{\rho_i}{\gamma} G_s \otimes_i I + \frac{\rho_w}{\gamma} G_s \otimes_o S + S^E - \frac{\rho_i}{\gamma} \overline{G_s \otimes_i I} - \frac{\rho_w}{\gamma} \overline{G_u \otimes_o S}. \tag{B.14}$$

The sea level equation in Equation B.14 is the form that is used within SELEN. to solve for the SLE numerically, a few more modifications are performed, but this is not within the scope of this research and this derivation can be found in Spada and Stocchi (2007).

B.2. Geoid Implementation Code

Below, the code is shown that reads the geoid file and assigns the geoid level to the Antarctic sea level field. The geoid file consist of the geoid levels from -120 000 years up to PD, with a timestep of 1 000 years. The ANICE program has an interval of 100 years, which is why the geoid is interpolated when the timestep is not a full thousand years (e.g. 117 000 years or 28 000 years).

```
IF (.NOT. C%use_geoid_forcing) THEN
deltaS_ant = Delta_Slev
ELSE IF (C%use_geoid_forcing)  THEN
    !every 1000 years the geoid gets called

    IF(MOD(time_loop_nr-1,10) == 0) THEN
        !if time is a full thousand, only call the current geoid
        CALL get_geoid(geoid_file,(time_loop_nr+9)/10,geoid_instance_past)
        !prevent call when in last thousand years
        !can't call geoid from future
        IF (((time_loop_nr+9)/10)+1 < 122) THEN
            CALL get_geoid(geoid_file,((time_loop_nr+9)/10)+1,geoid_instance_future)
        ENDIF
    END IF
    ! do interpolation here
    ! divine interpolation value
    geoid_divider = mod(time_loop_nr-1,10)
    geoid_divider = geoid_divider/10
    ! prevent call in last thousand years
    IF (((time_loop_nr+9)/10)+1 < 122) THEN
        geoid_instance = ((1-geoid_divider)*geoid_instance_past) + (geoid_divider*geoid_instance_future)
    ELSE
        geoid_instance = geoid_instance_past
    END IF
    ! set antarctic sea level to the geoid
    deltaS_ant = geoid_instance
END IF
END IF

WRITE (0,*) 'Inverse_coupling_program: CALL Antarctica grice routine'

CALL main_ant_grice_model(Delta_Temp + Temp_areaNH, dHb_dt_ant, deltaS_ant, hsl_ant, meaniso_ant, hsliso_
```

C

Relaxation Time Determination Method

The input for this method is the deflection curve that is the output of the normal model. The normal mode model was run for each location, where each location was subject to five different wavelengths. For two locations the deflection curves are shown in Figure C.1. In this figure, the deflection curves are shown for the NAP (a) and Amundsen (b) region. The curves for the EAIS, Ross, and Ronne regions are not shown here. The model starts at $t = 0$ at maximum deflection -the loading and bedrock are in equilibrium- where after $t = 0$ the loading disappears and the model runs up to $t = 15$ kyr during which the bedrock relaxes towards zero deflection. It can be seen that the larger wavelengths cause larger deflection. Furthermore, the curves show a semi-exponential fashion of relaxation.

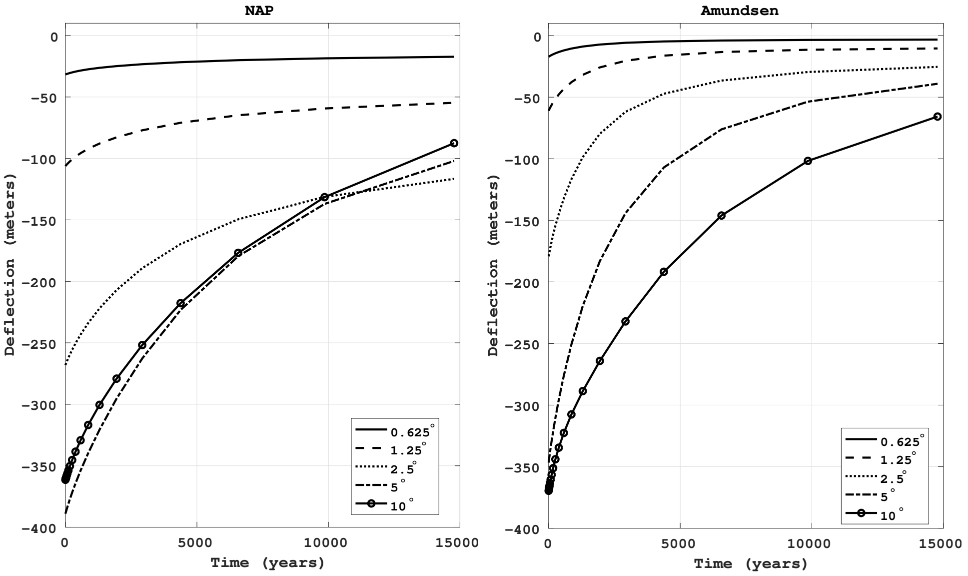

(a) (b)

Figure C.1: Bedrock uplift curves produced by the normal mode model for the NAP (a) and Amundsen (b) region.

As an example, one curve will be highlighted and the method will be explained. The curve that will be discussed is the 2.5° wavelength curve from the Amundsen region. This relaxation curve has interesting properties as it does not show the expected exponential behaviour. The normal mode model does not necessarily prescribe exponential relaxation, as the model features 5 layers with different viscosities which results in a complex rebound signal. The curve (dotted) is shown again in Figure C.2a, together with an exponential fit with a relaxation time of 12 000 years. The normal model curve does not fit the pure exponential, as it does not decreases to zero as the exponential curve does. In contrary, it behaves exponentially in the first 5000 years, but after this point, a second, slower exponential takes over. This is in agreement with the fact that the normal mode model features multiple viscosity layers and an complex uplift signal is expected. Here we see the 'fast' exponential during the first 5000 years, and a slower exponential signal taking over.

In order to fit an exponential curve to the complex exponential signal, a first approximation is done by trying to fit the original normal mode curve to an exponential curve, as in Figure C.2a, where an exponential curve with a relaxation time of 12 000 kyr is shown. However, it is shown that both the fast as well as the slow signal are not fitted accordingly. The speed of the fast signal is underestimated by the exponential fit, whereas the speed of the slow signal is overestimated by the exponential fit.

In order to make an accurate fit, the normal mode signal is filtered to attenuate the slow signal. This is done by visually estimating at what point in time the slow signal dominates the normal mode signal, and setting this as the zero-level for the fast rebound signal. The simple exponential form in Equation C.1 shows the exponential equation to which the curve is fitted. b is here the zero level for the fast rebound signal.

$$h(t) = exp(t/\tau) + b. \tag{C.1}$$

In Figure C.2b, the normal mode model curve is fitted to an purely exponential curve with $b = -130$. For the first 7000 years, the fit is in agreement with the normal model curve. After 7000 year, the normal model curve slow signal dominates, and the fit-error becomes larger.

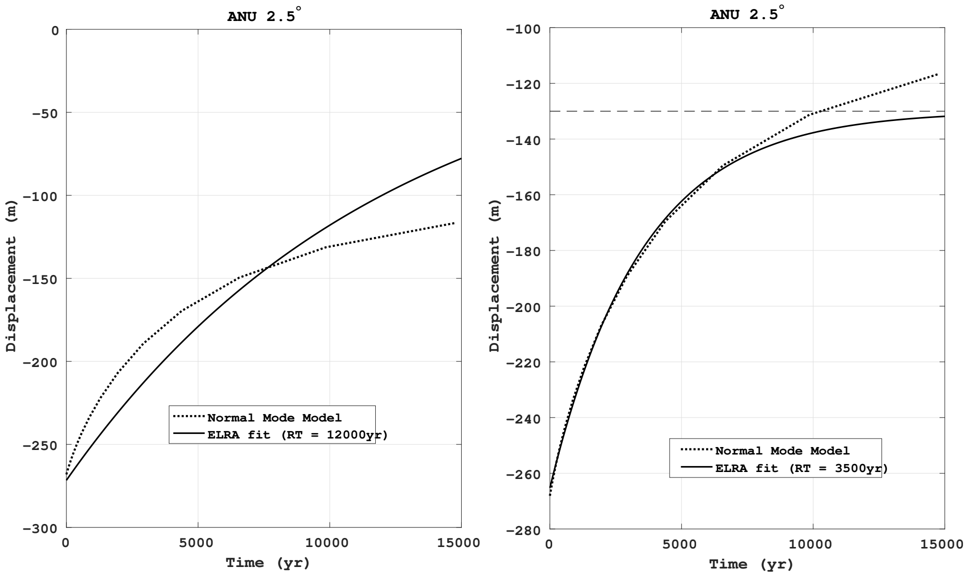

(a) (b)

Figure C.2: Bedrock uplift curves produced for the Amundsen region by the normal mode model and an exponential fit. (a) shows the fit with relaxation time of 12 kyr. (b) shows the fit with a relaxation time of 3500 years, but with a correction term applied.

D

Adaptive Relaxation Time Routine for ANICE

In this appendix, the adaptive relaxation time module will be discussed. The adaptive relaxation time module is build into the bedrock module of the ANICE program by (De Boer, 2014). The BED subroutine of the BEDROCK_ANT_MODULE module is displayed below in parts. It will be discussed part by part. The method showed in the code is described in section 4.4.

The subroutine has as input the ice height Hi, the bedrock height Hb, sealevel sealevel, the calve mask calve_mask. The output is the new bedrock height Hb_new. Next to these input variables, it uses several reference fields that are loaded in line 10: the ice height at t=0, Hi_ref, the region subdivision as in Figure 4.1 region_mask_ant. The relaxation time table RT_pippa where relaxation times are stored per wavelength and region. Taulat_ref is the original relaxation time file.

```
1   SUBROUTINE bed(Hi, Hb, sealevel, Hb_new, calve_mask)
2     ! Calculation of the new bedrock height.
3     ! See: Annals of Glaciology 23, 1996. E. LeMeur, and P. Huybrechts (1996):
4     ! A comparison of different ways of dealing with isostasy: examples from modelling the
5     ! Antarctic ice sheet during the last glacial cycle. Ann. Glaciol. 23, 309-317.
6
7     ! Hb is a level, it is the boundary between the bedrock and the ocean or ice above. Hb is often
8     ! compared with sealevel, because sealevel is relative to pd_sealevel, Hb must be relative to
9     ! pd_sealevel as well. (This means that large parts of the Hb-field contain negative values.)
10    USE reference_fields_ant_module, ONLY: Taulat_ref,  Hi_ref  , RT_pippa , region_mask_ant
! Relaxation time scale for bedrock adjustment
11    IMPLICIT NONE
12
13    ! Input variables:
14    INTEGER, DIMENSION(C%NX_ant,C%NY_ant), INTENT(IN)   :: calve_mask
! calve mask at time t
15    REAL(dp), DIMENSION(C%NX_ant,C%NY_ant), INTENT(IN)   :: Hi
! The ice_thickness at time t [m]
```

```
16     REAL(dp), DIMENSION(C%NX_ant,C%NY_ant), INTENT(IN)   :: Hb
   ! The bedrock height level at time t, relative to pd_sealevel [m]
17     REAL(dp), DIMENSION(C%NX_ant,C%NY_ant) :: Hi_corrected       ! The ice_thickness at time t [m]
18
19     REAL(dp),                               INTENT(IN)   :: sealevel ! The sealevel at time t, &
20      relative to pd_sealevel [m]
21
22     ! Output variables:
23     REAL(dp), DIMENSION(C%NX_ant,C%NY_ant), INTENT(OUT)  :: Hb_new
   ! The bedrock height level at time t + dt,
24                        !relative to pd_sealevel [m]
```

The next part, is where the modifications are mostly done. The skipped lines are comments explaining how the ELRA models works and are left out. In the code below, a few additional variables are declared that are used in the wavelength determination and relaxation time interpolation. The comments in the code are self-explanatory and will not be discussed here.

```
128     ! LOCATIONS
129     !1. Amundsen; 2. EA; 3. NAP; 4. Siple; 5. Wedell
130     !6. Wedell/NAP; 7. Wedell/NAP/Amundsen; 8. NAP/Amundsen;
131     !9. Amundsen/Wedell/Siple; 10. Amundsen/Siple 1/4
132
133 ! allocate vars:
134     REAL, DIMENSION(141,141):: Taulat_ref_smooth ! smoothed relaxation time field
135     REAL, DIMENSION(500,2)   :: list ! list with indices of borderelements
136     REAL, DIMENSION(5)       :: sizes_wl =(/ 0.625, 1.25, 2.5, 5.0, 10.0 /) !wavelengths for rt_vals
137     REAL, DIMENSION(5)       :: dist = (/ 0, 0, 0, 0, 0/) !array with max distance per lcocation
138     REAL, DIMENSION(5)       :: rem,RT_array !array with relaxation values per region for output
139     REAL, DIMENSION(2)       :: remsmall !used for interpolation
140     REAL, DIMENSION(1)       :: interpolatedRT ! interpolated relaxation time
141     REAL                     :: distnew = 0!,distance initializes as 0
142
143     INTEGER :: smootherx_top,smootherx_bot,smoothery_left,smoothery_right,&
144      loc,i,j,indlow,indhigh,listnumber = 0
145
146 ! only run through these steps if we want to use the Pippa models with adaptive wavelength determination
```

The next code snippet shows the wavelength determination. The complete method is explained in section 4.4. For each location the code is run. At line 154, the Hi_corrected field is initialised by subtracting the current ice height field Hi by the initial ice height field Hi_ref. The remaining field is set to zero for points where the ice is not grounded, not in the specific region, or where the ice height is below zero. From line 164 to 179, all points that lay on the boundary of the remaining region are stored in the list variable. The next part, from line 182 to 195, finds the largest distance among every possible combination of border points, and storing the maximum distance in dist. The dist array contains the maximum distance for each location. The distance is then converted to degrees wavelength by multiplying by the grid-distance divided by the arc-length of one degree on the surface of the earth.

```
147
148     IF (C%use_pippa_model) THEN
149
150     ! For each of the five locations
```

```
151     DO loc = 1,5
152         !initialize listnumber and hi_corrected
153         listnumber = 0
154         Hi_corrected  = Hi - Hi_ref
155 
156         ! remove -120kyr Hi from current Hi
157         ! Secondly, set all points to zero where the ice is NOT grounded
158         ! Thirdly, set all points to zero where the ice height is below zero
159         WHERE (.NOT. calve_mask == 1)            Hi_corrected = 0
160         WHERE (.NOT. region_mask_ant == loc)     Hi_corrected = 0
161         WHERE (Hi_corrected < 0)                 Hi_corrected = 0
162 
163         ! Find the points that are on the border of the remaining locations
164         DO i = 2,140
165             DO j = 2,140
166                 ! only look at points that are non-zero
167                 IF (.NOT. Hi_corrected(i,j) == 0) THEN
168                     ! find non-zero points that have neighbouring zero points
169                     ! if a element has more than or equal to 2 borderpoints that are zero,&
170                     ! they are considered an island and will not be considered as border point
171                     IF ( (any(Hi_corrected(i-1:i+1,j-1:j+1)==0)) .AND. &
172                         (count(Hi_corrected(i-1:i+1,j-1:j+1)==0) < 2) ) THEN
173                         ! add number to listnumber and store indicies in list
174                         listnumber = listnumber+1
175                         list(listnumber,:) = (/i,j/)
176                     END IF
177                 END IF
178             END DO !DO i = 2,140
179         END DO !j = 2,140
180 
181         ! find largest distance between all saved points in list
182         DO  i = 1,listnumber
183             DO j = i,listnumber
184             ! compute cartesian length
185                 distnew = SQRT( ((list(i,1) - list(j,1))**2) + ((list(i,2) - list(j,2))**2) );
186                 IF (distnew > dist(loc)) THEN
187                     dist(loc) = distnew;
188                 END IF
189             END DO !DO  i = 1,listnumber
190         END DO !DO j = i,listnumber
191 
192         ! check if longest distance is not
193         IF (dist(loc) < 1) THEN
194             dist(loc) = 1 ! minimum size of ice cap is one gridpoint
195         END IF
196 
197         ! compute wavelength in degrees (here half wavelength)
198         dist(loc) = (dist(loc)*(40/111.3188))/2;
```

Now, the largest distance in computed, the interpolation is done to find the correct wavelength. As FORTRAN does not feature an intrinsic interpolation function, this is done manually. From line 200 to 216, the interpolation is done by finding where the determined wavelength lies w.r.t. the known wavelengths array $\mathrm{RT\_pippa} = [0.625,\ 1.25,\ 2.5,\ 5,\ 10]$. The weights are determined and at line 217 the relaxation time is determined by the actual interpolation, where it is stored in $\mathrm{RT\_array}$. At line 220 the field Taulat_ref is filled with the determined relaxation time for the all points that define the region.

```
        ! set list to zero
        list = list*0

        ! find where to interpolate
        rem =(sizes_wl-dist(loc))/dist(loc);
        indlow = count(rem<=0)
        indhigh = count(rem<=0)+1

        ! set to max/min size when wavelength is larger than 10 or smaller than 0.625
        IF (dist(loc) >= 10) THEN
            indhigh = 5
        ELSE IF (dist(loc) <= 0.625) THEN
            indlow = 1
        END IF
        ! do the interpolation
        remsmall = rem(indlow:indhigh);
        remsmall = abs(1-abs(remsmall/sum(abs(remsmall))))
        RT_array(loc) = RT_pippa(indlow,loc)*remsmall(1)+RT_pippa(indhigh,loc)*remsmall(2)

        ! fill location region with the determined RT
        WHERE (region_mask_ant == loc) Taulat_ref = RT_array(loc)


    END DO !DO loc = 1,5
```

In the following code snippet, the regions that do not have a pre-determined relaxation time set, are assigned a value that is the average of surrounding regions. Five of such regions exist that are an average of surrounding regions.

```
    ! here, determine relaxation time for regions not in region 1,2,3,4,5
    ! it is basicallly the mean of surrounding regions
    DO i = 6,10
        IF (i == 6)     THEN
            interpolatedRT = (RT_array(3) + RT_array(5))/2
        ELSE IF (i ==7)  THEN
            interpolatedRT = (RT_array(1) + RT_array(3) + RT_array(5))/3
        ELSE IF (i==8)   THEN
            interpolatedRT = (RT_array(1) + RT_array(3))/2
        ELSE IF (i==9)   THEN
            interpolatedRT = (RT_array(1) +RT_array(5)+ RT_array(4))/3
        ELSE IF (i==10)  THEN
            interpolatedRT = ( RT_array(1) + RT_array(4))/2
        END IF

        WHERE (region_mask_ant == i) Taulat_ref = interpolatedRT(1)
    END DO

! write wavelength and relaxation times to file
    WRITE(27111993,*) dist
    WRITE(27111992,*) RT_array
    CALL FLUSH(27111992)
```

```
222     CALL FLUSH(27111993)
```

In the next part of the code, the generated field with relaxation time values is being smoothed. This will generate a more physically relevant field without rapid jumps in relaxation time value. The mean value is computed taking into account a square area of 3 points in every direction, unless a point on the border of the map is considered. In that case, only the points up to the border are considered.

```
250     ! do smoothing here, each point get smoothed taking into account 6 points around the point
251     Taulat_ref_smooth = Taulat_ref*0
252     DO i = 1,141
253         smootherx_top = 3
254         smootherx_bot = 3
255         DO WHILE (smootherx_top >= i)
256             smootherx_top = smootherx_top - 1
257         END DO
258         DO WHILE (smootherx_bot > 141-i)
259             smootherx_bot = smootherx_bot - 1
260         END DO
261         DO j = 1,141
262             smoothery_left =3
263             smoothery_right =3
264             DO WHILE (smoothery_left >= j)
265                 smoothery_left = smoothery_left - 1
266             END DO
267             DO WHILE (smoothery_right > 141-j)
268                 smoothery_right = smoothery_right - 1
269             END DO
270
271
272             Taulat_ref_smooth(i,j) = sum(Taulat_ref(i-smootherx_top:i+smootherx_bot,j-
smoothery_left:j+smoothery_right))/ &
273                                        size(Taulat_ref(i-smootherx_top:i+smootherx_bot,j-
smoothery_left:j+smoothery_right))
274         END DO !DO j = 1,141
275     END DO !O i = 1,141
```

Here, the value Hb_new is computed in line 277 with the field Taulat_ref_smooth, which is the field with relaxation time values, but smoothed. In case the routine with adaptive relaxation time is not used, the Hb_new field is computed solely by using the standard relaxation time field, as in line 282.

```
277         Hb_new = Hb + (C%dt_bedrock / Taulat_ref_smooth) * (Hb_eq_pd + bedrock_deformation(Hb, Hi, sealevel) -
 Hb)
278     ELSE IF (.NOT. C%use_pippa_model) THEN !(C%use_pippa_model)
279         Hb_new = Hb + (C%dt_bedrock / Taulat_ref) * (Hb_eq_pd + bedrock_deformation(Hb, Hi, sealevel) -
 Hb)
280     END IF !(C%use_pippa_model)
281
282
283   END SUBROUTINE bed
```

Bibliography

An, M., Wiens, D. A., Zhao, Y., Feng, M., Nyblade, A. A., Kanao, M., Li, Y., Maggi, A., and Lévêque, J. J. (2015). S-velocity model and inferred Moho topography beneath the Antarctic Plate from Rayleigh waves. *Journal of Geophysical Research: Solid Earth*, 120(1):359–383.

Angevine, C. L., Heller, P. L., and Paola, C. (1990). *Quantitative Sedimentary Basin Modeling*. American Association of Petroleum Geologists.

Artemieva, I. M. and Mooney, W. D. (2001). Thermal thickness and evolution of Precambrian lithosphere: A global study. *Journal of Geophysical Research: Solid Earth*, 106(B8):16387–16414.

Bamber, J. L., Riva, R. E. M., Vermeersen, B. L. A., and LeBrocq, A. M. (2009). Reassessment of the Potential Sea-Level Rise from a Collapse of the West Antarctic Ice Sheet. *Science*, 324(5929):901–903.

Barnhoorn, A., van der Wal, W., and Drury, M. R. (2011). Upper mantle viscosity and lithospheric thickness under Iceland. *Journal of Geodynamics*, 52(3-4):260–270.

Bintanja, R., Van De Wal, R. S., and Oerlemans, J. (2002). Global ice volume variations through the last glacial cycle simulated by a 3-D ice-dynamical model. *Quaternary International*, 95-96:11–23.

Bueler, E. and Brown, J. (2009). Shallow shelf approximation as a ”sliding law” in a thermomechanically coupled ice sheet model. *Journal of Geophysical Research: Solid Earth*, 114(3).

Bunge, H.-P., Richards, M. A., and Baumgardner, J. R. (1996). Effect of depth-dependent viscosity on the planform of mantle convection. *Nature*, 379(6564):436–438.

Cammarano, F., Tackley, P., and Boschi, L. (2011). Seismic, petrological and geodynamical constraints on thermal and compositional structure of the upper mantle: Global thermochemical models. *Geophysical Journal International*, 187(3):1301–1318.

De Boer, B. (2014). ANICE Computer Model.

De Boer, B., Dolan, A. M., Bernales, J., Gasson, E., Goelzer, H., Golledge, N. R., Sutter, J., Huybrechts, P., Lohmann, G., Rogozhina, I., Abe-Ouchi, A., Saito, F., and Van De Wal, R. S. W. (2015). Simulating the Antarctic ice sheet in the late-Pliocene warm period: PLISMIP-ANT, an ice-sheet model intercomparison project. *Cryosphere*, 9(3):881–903.

de Boer, B., Stocchi, P., Whitehouse, P. L., and van de Wal, R. S. (2017). Current state and future perspectives on coupled ice-sheet – sea-level modelling.

De Boer, B., Van De Wal, R. S., Bintanja, R., Lourens, L. J., and Tuenter, E. (2010). Cenozoic global ice-volume and temperature simulations with 1-D ice-sheet models forced by benthic δ18O records. *Annals of Glaciology*, 51(55):23–33.

De Boer, B., van de Wal, R. S. W., Lourens, L. J., Bintanja, R., and Reerink, T. J. (2013). A continuous simulation of global ice volume over the past 1 million years with 3-D ice-sheet models. *Climate Dynamics*, 41(5-6):1365–1384.

Ehlers, J., Hughes, P., and Gibbard, P. (2015). *The Ice Age*. Wiley, Singapore, 1st edition.

Farrell, W. E. (1973). Earth Tides, Ocean Tides and Tidal Loading. *Philosophical Transactions of the Royal Society A: Mathematical, Physical and Engineering Sciences*, 274(1239):253–259.

Farrell, W. E. and Clark, J. A. (1976). On Postglacial Sea Level. *Geophysical Journal of the Royal Astronomical Society*, 46(3):647–667.

Feldmann, J. and Levermann, A. (2015). Collapse of the West Antarctic Ice Sheet after local destabilization of the Amundsen Basin. *Proceedings of the National Academy of Sciences*, 112(46):14191–14196.

Fjeldskaar, W. and Cathles, L. (1991). *Rheology of Mantle and Lithosphere Inferred from Post-Glacial Uplift in Fennoscandia*, pages 1–19. Springer Netherlands, Dordrecht.

Forte, A. M., Dziewonski, A. M., and O'Connell, R. J. (1995). Continent-ocean chemical heterogeneity in the mantle based on seismic tomography. *Science*, 268(5209):386–388.

Fowler, A. (2011). *Mathematical Geoscience*, volume 36. Springer, London, 1st edition.

Fretwell, P., Pritchard, H. D., Vaughan, D. G., Bamber, J. L., Barrand, N. E., Bell, R., Bianchi, C., Bingham, R. G., Blankenship, D. D., Casassa, G., Catania, G., Callens, D., Conway, H., Cook, A. J., Corr, H. F., Damaske, D., Damm, V., Ferraccioli, F., Forsberg, R., Fujita, S., Gim, Y., Gogineni, P., Griggs, J. A., Hindmarsh, R. C., Holmlund, P., Holt, J. W., Jacobel, R. W., Jenkins, A., Jokat, W., Jordan, T., King, E. C., Kohler, J., Krabill, W., Riger-Kusk, M., Langley, K. A., Leitchenkov, G., Leuschen, C., Luyendyk, B. P., Matsuoka, K., Mouginot, J., Nitsche, F. O., Nogi, Y., Nost, O. A., Popov, S. V., Rignot, E., Rippin, D. M., Rivera, A., Roberts, J., Ross, N., Siegert, M. J., Smith, A. M., Steinhage, D., Studinger, M., Sun, B., Tinto, B. K., Welch, B. C., Wilson, D., Young, D. A., Xiangbin, C., and Zirizzotti, A. (2013). Bedmap2: Improved ice bed, surface and thickness datasets for Antarctica. *Cryosphere*, 7(1):375–393.

Geruo, A., Wahr, J., and Zhong, S. (2013). Computations of the viscoelastic response of a 3-D compressible earth to surface loading: An application to glacial isostatic adjustment in Antarctica and Canada. *Geophysical Journal International*, 192(2):557–572.

Goes, S., Govers, R., and Vacher, P. (2000). Shallow mantle temperatures under Europe from P and S wave tomography. *Journal Of Geophysical Research-Solid Earth*, 105(B5):11153–11169.

Gomez, N., Pollard, D., and Holland, D. (2015). Sea-level feedback lowers projections of future Antarctic Ice-Sheet mass loss. *Nature Communications*, 6.

Gomez, N., Pollard, D., and Mitrovica, J. X. (2013). A 3-D coupled ice sheet - sea level model applied to Antarctica through the last 40 ky. *Earth and Planetary Science Letters*, 384:88–99.

Greve, R. and Blatter, H. (2013). Greve and Blatter (2009), Dynamics of Ice Sheets and Glaciers: Errata. (2009):0–3.

Groh, A., Ewert, H., Scheinert, M., Fritsche, M., Rülke, A., Richter, A., Rosenau, R., and Dietrich, R. (2012). An investigation of Glacial Isostatic Adjustment over the Amundsen Sea sector, West Antarctica. *Global and Planetary Change*, 98-99:45–53.

Heeszel, D. S., Wiens, D. A., Anandakrishnan, S., Aster, R. C., Dalziel, I. W., Huerta, A. D., Nyblade, A. A., Wilson, T. J., and Winberry, J. P. (2016). Upper mantle structure of central and West Antarctica from array analysis of Rayleigh wave phase velocities. *Journal of Geophysical Research: Solid Earth*, 121(3):1758–1775.

Hirth, G. and Kohlstedt, D. (2003). Rheology of the upper mantle and the mantle wedge: A view from the experimentalists. *Washington DC American Geophysical Union Geophysical Monograph Series*, 138:83–105.

Huybrechts, P. (1990). A 3-D model for the Antarctic ice sheet: a sensitivity study on the glacial-interglacial contrast. *Climate Dynamics*, 5(2):79–92.

Huybrechts, P. (2002). Sea-level changes at the LGM from ice-dynamic reconstructions of the Greenland and Antarctic ice sheets during the glacial cycles. *Quaternary Science Reviews*, 21(1-3):203–231.

Ivins, E. R. and Sammis, C. G. (1995). On lateral viscosity contrast in the mantle and the rheology of low□frequency geodynamics. *Geophysical Journal International*, 123(2):305–322.

Janssens, I. and Huybrechts, P. (2000). The treatment of meltwater retention in mass-balance parameterizations of the Greenland ice sheet.

Jordan, T. H. (1978). Composition and development of the continental tectosphere. *Nature*, 274(5671):544–548.

Joughin, I., Smith, B. E., and Medley, B. (2014). Marine Ice Sheet Collapse Potentially Under Way for the Thwaites Glacier Basin, West Antarctica. *Science*, 344(6185):735–738.

Karato, S.-i. (2008). *Deformation of Earth Materials: An Introduction to the Rheology of Solid Earth*, volume 463.

Kaufmann, G. and Lambeck, K. (2002). Glacial isostatic adjustment and the radial viscosity profile from inverse modeling. *Journal of Geophysical Research: Solid Earth*, 107(B11):ETG 5–1–ETG 5–15.

Kaufmann, G., Wu, P., and Ivins, E. R. (2005). Lateral viscosity variations beneath Antarctica and their implications on regional rebound motions and seismotectonics. *Journal of Geodynamics*, 39(2):165–181.

Kearey, P., Klepeis, K. a., and Vine, F. J. (2009). *Global tectonics*, volume 168.

L. Kirschvink, J. (1992). Late Proterozoic Low-Latitude Global Glaciation: The Snowball Earth. *The Proterozoic Biosphere: A Multidisciplinary Study*.

Lambeck, K., Johnston, P., and Nakada, M. (1990). Holocene glacial rebound and sea□level change in NW Europe. *Geophysical Journal International*, 103(2):451–468.

Le Meur, E. (1996). Isostatic postglacial rebound over Fennoscandia with a self-gravitating spherical visco-elastic Earth model. *Annals of Glaciology*, 23.

Le Meur, E. and Hindmarsh, R. C. A. (2001). Coupled marine-ice-sheet/Earth dynamics using a dynamically consistent ice-sheet model and a self-gravitating viscous Earth model. *Journal of Glaciology*, 47(157):258–270.

Le Meur, E. and Huybrechts, P. (1996). A comparisonon if different ways of dealing with isostasy: Examples from modelling the Antarctic ice sheet during the last grlacial cycle.

Liggett, D., Storey, B., and Cook, Y. (2016). Exploring the last continent: An introduction to Antarctica. In *Exploring the Last Continent: An Introduction to Antarctica*, pages 1–6.

MacAyeal, D. R. (1989). Large-scale ice flow over a viscous basal sediment: Theory and application to ice stream B, Antarctica.

Martin, M. A., Winkelmann, R., Haseloff, M., Albrecht, T., Bueler, E., Khroulev, C., and Levermann, A. (2011). The Potsdam Parallel Ice Sheet Model (PISM-PIK) - Part 2: Dynamic equilibrium simulation of the Antarctic ice sheet. *Cryosphere*, 5(3):727–740.

McConnell Jr, R. K. (1965). Isostatic adjustment in a layered earth. *J Geophys Res*, 70(20):5171–5188.

Mercer, J. H. (1978). West Antarctic ice sheet and CO2 greenhouse effect: A threat of disaster. *Nature*, 271(5643):321–325.

Morelli, A. and Danesi, S. (2004). Seismological imaging of the Antarctic continental lithosphere: A review. In *Global and Planetary Change*, volume 42, pages 155–165.

Muller, R. A. and MacDonald, G. J. (2000). *Ice Ages and Astronomical Causes*. Springer - Praxis, Chichester, 1st edition.

Nield, G. A., Barletta, V. R., Bordoni, A., King, M. A., Whitehouse, P. L., Clarke, P. J., Domack, E., Scambos, T. A., and Berthier, E. (2014). Rapid bedrock uplift in the Antarctic Peninsula explained by viscoelastic response to recent ice unloading. *Earth and Planetary Science Letters*.

Pasyanos, M. E. (2010). Lithospheric thickness modeled from long-period surface wave dispersion. *Tectonophysics*, 481(1-4):38–50.

Pattyn, F. (2003). A new three-dimensional higher-order thermomechanical ice sheet model: Basic sensitivity, ice stream development, and ice flow across subglacial lakes. *Journal of Geophysical Research*, 108(B8):1–15.

Peltier, W. (2004). GLOBAL GLACIAL ISOSTASY AND THE SURFACE OF THE ICE-AGE EARTH: The ICE-5G (VM2) Model and GRACE. *Annual Review of Earth and Planetary Sciences*, 32(1):111–149.

Peltier, W. R. (1974). The impulse response of a Maxwell Earth. *Reviews of Geophysics*, 12(4):649.

Peltier, W. R. (1982). Dynamics of the ice age Earth. *Adv. Geophys*, 24:1–146.

Pollard, D. and Deconto, R. M. (2009). Modeling West Antarctic ice sheet growth and collapse through the past five million years. *Nature*, 458:329–332.

Pollard, D. and DeConto, R. M. R. (2007). A Coupled Ice-Sheet/Ice-Shelf/Sediment Model Applied to a Marine-Margin Flowline: Forced and Unforced Variations. *Glacial sedimentary processes and products*, (August):37–52.

Sabadini, R., Yuen, D. A., and Portney, M. (1986). The effects of upper□mantle lateral heterogeneities on postglacial rebound. *Geophysical Research Letters*, 13(4):337–340.

Scambos, T. A., Bohlander, J. A., Shuman, C. A., and Skvarca, P. (2004). Glacier acceleration and thinning after ice shelf collapse in the Larsen B embayment, Antarctica. *Geophysical Research Letters*, 31(18).

Schaeffer, A. J. and Lebedev, S. (2013). Global shear speed structure of the upper mantle and transition zone. *Geophysical Journal International*, 194(1):417–449.

Schoof, C. (2007). Ice sheet grounding line dynamics: Steady states, stability, and hysteresis. *Journal of Geophysical Research: Earth Surface*, 112(3).

Schoof, C. and Hewitt, I. (2013). Ice-Sheet Dynamics. *Annual Review of Fluid Mechanics*, 45(1):217–239.

Spada, G., Antonioli, A., Cianetti, S., and Giunchi, C. (2006). Glacial isostatic adjustment and relative sea-level changes: The role of lithospheric and upper mantle heterogeneities in a 3-D spherical Earth. *Geophysical Journal International*, 165(2):692–702.

Spada, G., Barletta, V. R., Klemann, V., Riva, R. E. M., Martinec, Z., Gasperini, P., Lund, B., Wolf, D., Vermeersen, L. L. A., and King, M. A. (2011). A benchmark study for glacial isostatic adjustment codes. *Geophysical Journal International*, 185(1):106–132.

Spada, G. and Stocchi, P. (2007). SELEN: A Fortran 90 program for solving the ”sea-level equation”. *Computers and Geosciences*.

Thomas, R. (2004). Accelerated Sea-Level Rise from West Antarctica. *Science*, 306(5694):255–258.

van de Wal, R. S. W. (1999). The importance of thermodynamics for modeling the volume of the Greenland ice sheet. *Journal of Geophysical Research-Atmospheres*, 104(D4):3887–3898.

van den Berg, J., van de Wal, R., and Oerlemans, H. (2008a). A mass balance model for the Eurasian Ice Sheet for the last 120,000 years. *Global and Planetary Change*, 61:194–208.

van den Berg, J., van de Wal, R. S. W., Milne, G. A., and Oerlemans, J. (2008b). Effect of isostasy on dynamical ice sheet modeling: A case study for Eurasia. *Journal of Geophysical Research: Solid Earth*, 113(5):1–13.

van den Berg, J., Van de Wal, R. S. W., and Oerlemans, J. (2006). Effects of spatial discretization in ice-sheet modelling using the shallow-ice approximation. *Journal of Glaciology*, 52(176):89–98.

van der Veen, C. (1999). *Fundamentals of Glacier Dynamics*. CRC Press.

Van Der Wal, W., Barnhoorn, A., Stocchi, P., Gradmann, S., Wu, P., Drury, M., and Vermeersen, B. (2013). Glacial isostatic adjustment model with composite 3-D Earth rheology for Fennoscandia. *Geophysical Journal International*, 194(1):61–77.

van der Wal, W., Whitehouse, P. L., and Schrama, E. J. O. (2015). Effect of GIA models with 3D composite mantle viscosity on GRACE mass balance estimates for Antarctica. *Earth and Planetary Science Letters*, 414:134–143.

Weertman, J. (1974). Stability of the junction of an ice sheet and an ice shelf. *Journal of Glaciology*, 13(67):3–11.

Whitehouse, P. L., Bentley, M. J., and Le Brocq, A. M. (2012). A deglacial model for Antarctica: Geological constraints and glaciological modelling as a basis for a new model of Antarctic glacial isostatic adjustment. *Quaternary Science Reviews*, 32:1–24.

Whitehouse, P. L., Bentley, M. J., Vieli, A., Jamieson, S. S., Hein, A. S., and Sugden, D. E. (2017a). Controls on Last Glacial Maximum ice extent in the Weddell Sea embayment, Antarctica. *Journal of Geophysical Research: Earth Surface*, 122(1):371–397.

Whitehouse, P. L., van der Wal, W., King, M. A., Wiens, D. A., and Wilson, T. J. (2017b). Ice mass change during last 4000 years dominates West Antarctic Glacial Isostatic Adjustment signal. Manuscript in preparation.

Woodward, R. S. (1888). On the form and position of the sea level with special references to its dependence on superficial masses symmetrically disposed about a normal to the earth's surface. Technical report.

Wu, P. and Peltier, W. R. (1982). Viscous gravitational relaxation. *Geophysical Journal of the Royal Astronomical Society*, 70(2):435–485.

Wu, P. and Peltier, W. R. (1983). Glacial isostatic adjustment and the free air gravity anomaly as a constraint on deep mantle viscosity. *Geophysical Journal of the Royal Astronomical Society*, 74(2):377–449.

Wu, P., Wang, H., and Steffen, H. (2013). The role of thermal effect on mantle seismic anomalies under laurentia and fennoscandia from observations of glacial isostatic adjustment. *Geophysical Journal International*, 192(1):7–17.